

THE LYMAN-ALPHA REFERENCE SAMPLE: I. SURVEY OUTLINE AND FIRST RESULTS FOR MARKARIAN 259

GÖRAN ÖSTLIN², MATTHEW HAYES², FLORENT DUVAL², ANDREAS SANDBERG², THØGER RIVERA-THORSEN², THOMAS MARQUART^{2,3}, IVANA ORLITOVÁ^{4,14}, ANGELA ADAMO², JENS MELINDER², LUCIA GUAITA², HAKIM ATEK⁵, JOHN M. CANNON⁶, PIETER GRUYTERS³, EDMUND CHRISTIAN HERENZ⁷, DANIEL KUNTH⁸, PETER LAURSEN^{2,9}, J. MIGUEL MAS-HESSE¹⁰, GENOVEVA MICHEVA^{2,11}, HÉCTOR OTÍ-FLORANES^{12,13}, STEPHEN A. PARDY^{6,13}, MARTIN M. ROTH⁷, DANIEL SCHÄFER⁴, AND ANNE VÉRHAMME⁴

Draft version June 30, 2018

ABSTRACT

The Lyman-alpha reference sample (LARS) is a substantial program with the Hubble Space Telescope (HST) that provides a sample of local universe laboratory galaxies in which to study the detailed astrophysics of the visibility and strength of the Lyman-alpha ($\text{Ly}\alpha$) line of neutral hydrogen. $\text{Ly}\alpha$ is the dominant spectral line in use for characterizing high redshift (z) galaxies. This article presents an overview of the survey, its selection function and HST imaging observations. The sample was selected from the combined GALEX+SDSS catalogue at $z = 0.028 - 0.19$, in order to allow $\text{Ly}\alpha$ to be captured with combinations of long pass filters in the Solar Blind Channel (SBC) of the Advanced Camera for Surveys (ACS) on board HST. In addition, LARS utilises $\text{H}\alpha$ and $\text{H}\beta$ narrow, and u, b, i broad-band imaging with ACS and the Wide Field Camera 3 (WFC3). In order to study galaxies in which large numbers of $\text{Ly}\alpha$ photons are produced (whether or not they escape) we demanded an $\text{H}\alpha$ equivalent width $W(\text{H}\alpha) \geq 100\text{\AA}$. The final sample of 14 galaxies covers far UV (FUV, $\lambda \sim 1500\text{\AA}$) luminosities that overlaps with those of high- z $\text{Ly}\alpha$ emitters and Lyman Break Galaxies (LBGs), making LARS a valid comparison sample. We present the reduction steps used to obtain the $\text{Ly}\alpha$ images, including our LARS eXtraction software (LaXs) which utilises pixel-by-pixel spectral synthesis fitting of the energy distribution to determine and subtract the continuum at $\text{Ly}\alpha$. We demonstrate that the use of SBC long pass filter combinations increase the signal to noise with an order of magnitude compared to the nominal $\text{Ly}\alpha$ filter available in SBC. To exemplify the science potential of LARS, we also present some first results for a single galaxy, Mrk 259 (LARS #1). This irregular galaxy shows bright extended (indicative of resonance scattering), but strongly asymmetric $\text{Ly}\alpha$ emission. Spectroscopy from HST/COS centered on the brightest UV knot show a moderate outflow in the neutral interstellar medium (probed by low ionization stage absorption features), and $\text{Ly}\alpha$ emission with an asymmetric profile. Radiative transfer modeling is able to reproduce the essential features of the $\text{Ly}\alpha$ line profile, and confirms the presence of an outflow. From the integrated photometry we measure a $\text{Ly}\alpha$ luminosity of $L_{\text{Ly}\alpha} = 1.3 \times 10^{42}$ erg/s an equivalent width $W(\text{Ly}\alpha) = 45\text{\AA}$ and a far UV absolute magnitude $M_{\text{FUV}} = -19.2$ (AB). Mrk 259 would hence be detectable in high- z $\text{Ly}\alpha$ and LBG surveys. The total $\text{Ly}\alpha$ escape fraction is 12 %. This number is higher than the low- z average, but similar to that at $z > 4$ demonstrating that LARS provides a valid comparison sample for high- z galaxy studies.

Subject headings: cosmology: observations — galaxies: star-burst — galaxies: individual (Mrk 259)

¹ Based on observations made with the NASA/ESA Hubble Space Telescope, obtained at the Space Telescope Science Institute, which is operated by the Association of Universities for Research in Astronomy, Inc., under NASA contract NAS 5-26555. These observations are associated with program #12310,#11522.

² Department of Astronomy, Stockholm University, Oscar Klein Centre, AlbaNova, Stockholm SE-106 91, Sweden

³ Department of Physics and Astronomy, Division of Astronomy and Space Physics, Uppsala University, Box 516, 75120 Uppsala, Sweden

⁴ Observatoire de Genève, Université de Genève, Chemin des Maillettes 51, 1290 Versoix, Switzerland

⁵ Laboratoire d'Astrophysique, Ecole Polytechnique Fédérale de Lausanne, Observatoire de Sauverny, CH-1290 Versoix, Switzerland

⁶ Department of Physics & Astronomy, Macalester College, 1600 Grand Avenue, Saint Paul, MN 55105

⁷ Leibniz-Institute for Astrophysics Potsdam (AIP), innoF-SPEC, An der Sternwarte 16, 14482 Potsdam, Germany

⁸ Institut d'Astrophysique Paris, 98bis Bd Arago, 75014 Paris

⁹ Dark Cosmology Centre, Niels Bohr Institute, University of Copenhagen, DK-2100, Denmark

¹⁰ Centro de Astrobiología (CSIC-INTA), Departamento de Astrofísica, POB 78, 28691, Villanueva de la Cañada, Spain

¹¹ Subaru Telescope, National Astronomical Observatory of Japan, 650 North A'ohoku Place, Hilo, HI 96720, U.S.A.

¹² Instituto de Astronomía, Universidad Nacional Autónoma de México, Apdo. Postal 106, Ensenada B. C. 22800, Mexico

¹³ University of Wisconsin - Madison, 475 N. Charter Street, Madison, WI 53706, USA

¹⁴ Astronomical Institute, Academy of Sciences of the Czech Republic, Boří II 1401, 141 00 Prague, Czech Republic.

¹⁵ Centro de Radioastronomía y Astrofísica, UNAM, Campus Morelia, Mexico

1. INTRODUCTION

The Lyman-alpha emission line ($\text{Ly}\alpha$) fulfills several extremely important roles in observations of the high-redshift (z) universe. Firstly, as recombination nebulae re-process $\sim 1/3$ of the raw ionizing power of hot stars into a single narrow ($\sim 1\text{\AA}$) spectral emission feature, it acts as a luminous spectral beacon by which to identify galaxies at the highest redshifts (Hu & McMahon 1996; Cowie & Hu 1998; Malhotra & Rhoads 2002; van Breukelen et al. 2005; Gawiser et al. 2006; Shimasaku et al. 2006; Nilsson et al. 2007; Ouchi et al. 2008; Hayes et al. 2010; Adams et al. 2011). Secondly, at the highest redshift it provides at least the potential for the all-important spectroscopic confirmation of galaxies selected by other methods, transforming the status of candidates to objects with secure redshifts (Steidel et al. 1996; Chapman et al. 2005; Vanzella et al. 2009; Stark et al. 2010; Lehnert et al. 2010; Curtis-Lake et al. 2012).

$\text{Ly}\alpha$ is also a resonance line and photons may scatter wherever they encounter neutral hydrogen atoms. This scattering may occur in the interstellar medium (ISM) of the galaxies themselves, or after emission from galaxies, in the intergalactic medium (IGM) that immediately surrounds them. Inside the ISM, this resonance scattering leads to a complicated radiative transport of $\text{Ly}\alpha$, in which the visibility of the line may be influenced by large number of factors, including raw dust content (Charlot & Fall 1993; Verhamme et al. 2008a; Atek et al. 2009; Hayes et al. 2010; Atek et al. 2014), dust geometry (Scarlata et al. 2009), the neutral gas content and kinematics (Kunth et al. 1998; Mas-Hesse et al. 2003), and gas geometry (Neufeld 1991; Giavalisco et al. 1996; Hansen & Oh 2006; Laursen et al. 2013; Duval et al. 2014). These radiative transport issues, and the fact that to date no clear order of precedence has been established between them (although see Mallory et al. 2012), implies that the total escape fraction of $\text{Ly}\alpha$ photons ($f_{\text{esc}}^{\text{Ly}\alpha}$; defined as the ratio of observed to intrinsic $\text{Ly}\alpha$ luminosity; Hayes et al. 2005), cannot be predicted from knowledge of any single of the above quantities. The direct consequence of this is that photometric measurements of $\text{Ly}\alpha$ will reflect the underlying properties of galaxies only in the very broadest statistical sense, and for individual galaxies, the observed $\text{Ly}\alpha$ flux would not reveal much about the underlying physical quantities. Moreover, if it is not understood what conditions that regulate galaxies' ability to emit the $\text{Ly}\alpha$ photons that are produced within them, studies of the galaxy population and cosmology by means of $\text{Ly}\alpha$ will be subject to unknown biases.

However, regarding the IGM the situation of $\text{Ly}\alpha$ -emission vis-a-vis radiative transport is not so pessimistic. Again due to the high absorption cross section in HI , $\text{Ly}\alpha$ observations provide an independent test of the intermediate to late stages of reionization (Haiman 2002; Santos 2004; Malhotra & Rhoads 2004; Verhamme et al. 2008a; Dijkstra & Wyithe 2010), where it is sensitive to intermediate volume-ionized fractions of a few 10 per-cent (Ouchi et al. 2008). In contrast the Gunn-Peterson trough observed in quasar absorption spectra (e.g. Fan et al. 2006) only probes the very final stages ($< 1\%$ neutral). Obviously these $\text{Ly}\alpha$ tests are reliant upon the condition that, at the highest redshifts, a substantial fraction of the $\text{Ly}\alpha$ photons that are produced

are able to avoid being trapped by their own ISM. While this condition seems not to be fulfilled at low and intermediate redshift (Cowie et al. 2010; Hayes et al. 2011) $\text{Ly}\alpha$ emission seems to undergo a strong cosmic evolution as evidenced by three primary results. With increasing z : (a) the volumetric $\text{Ly}\alpha$ escape fraction increases (Hayes et al. 2011); (b) the fraction of UV-selected galaxies with strong $\text{Ly}\alpha$ increases (Stark et al. 2010); and (3) the UV luminosity functions of UV- and $\text{Ly}\alpha$ -selected galaxies appear to converge (Ouchi et al. 2008). Thus the future of $\text{Ly}\alpha$ as a probe of reionization and of galaxy evolution in general may be an optimistic one if we can understand on what conditions a galaxy transmits its $\text{Ly}\alpha$ photons.

Recent years have seen considerable effort go into the modeling of $\text{Ly}\alpha$ transport using intensive computer simulations, working in idealized galaxy geometries (Dijkstra et al. 2006; Verhamme et al. 2006; Cantalupo & Porciani 2011), and quasi-realistic galaxies drawn from computer simulations (Tasitsiomi 2006; Laursen et al. 2009; Verhamme et al. 2012; Yajima et al. 2012). Results have been as insightful as they have been CPU-intensive but are still, taken as a whole, unsatisfactory. Regarding transport studies in simulated galaxies, it is not clear that galaxy formation models probe the necessary scales, that photons are injected in the correct places, that clumping of the ISM is realistic, or that dust production, destruction or coupling with metallicity necessarily conform with nature. Perhaps most important, simulated galaxies lack a realistic treatment of galactic winds. Regarding idealized geometries, it is not clear that sufficient parameter spaces are covered, if vital quantities are omitted, or whether distributions are realistic (particularly regarding the multiphase ISM). What is badly needed in this field is stronger empirical constraints on the $\text{Ly}\alpha$ transport process.

1.1. The case for low redshift $\text{Ly}\alpha$ imaging

$\text{Ly}\alpha$ is used intensively to study the galaxy population at high- z , and luminosity functions (LF; see compilation in Hayes et al. 2011) and equivalent width (EW) distributions are now becoming well populated (Gronwall et al. 2007; Ouchi et al. 2008; Stark et al. 2010). Yet while it is exactly these properties that are used to describe the high- z galaxy population, these galaxies all lie at distances too great for us to determine the physical processes that actually shape the aforementioned distributions. Notably standard nebular diagnostics of dust attenuation, metallicity, and ionization state are redshifted to wavelengths where they are difficult or impossible to observe, and that forces the community to turn to sub-optimal and biased observables/indices. Particularly for $\text{Ly}\alpha$ -selected galaxies, which typically exhibit faint stellar continua, measuring features like the 4000\AA break also becomes increasingly troublesome. Far UV absorption features (either interstellar or photospheric) may be visible but again, only for the brightest galaxies. These problems are typically solved through stacking analyses, which destroys almost all information relating to the diversity of the populations. Moreover, spatial sampling scales at high- z are around $6\text{--}8\text{ kpc/arcsec}$, meaning most high- z galaxies are unresolved in ground-based data and surface brightness, which decreases proportionally to $(1+z)^{3(4)}$ in an unresolved (resolved) emission

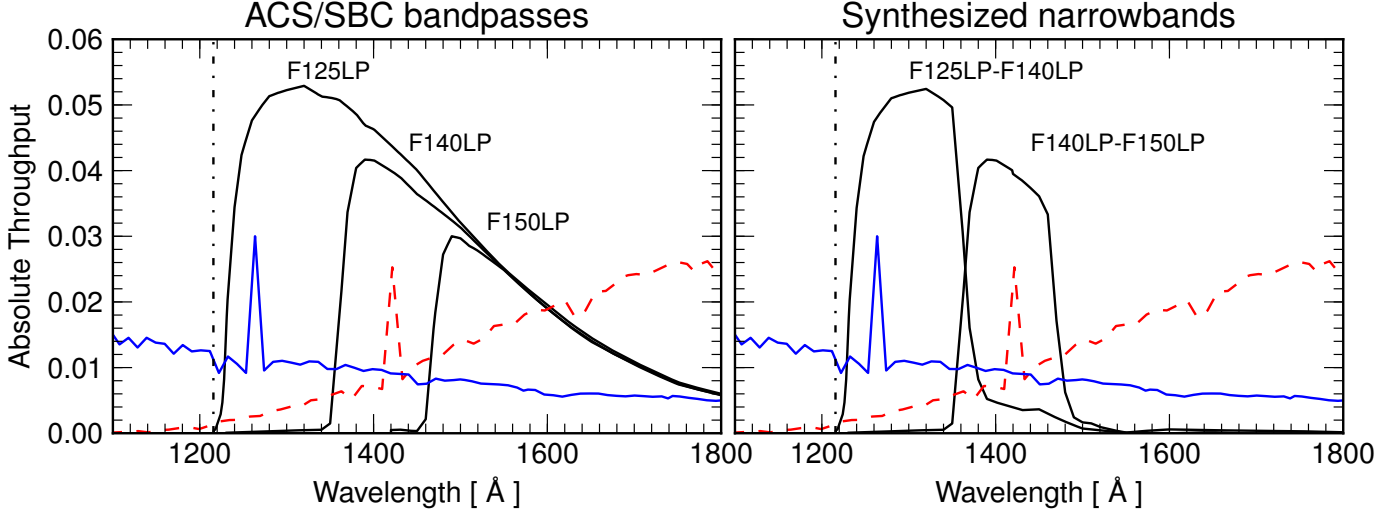


Figure 1. ACS/SBC bandpass combinations (left) that yield effective Ly α bandpasses (right). Bandpasses are labeled, as are the synthesized narrowbands that result from the subtraction of adjacent long-pass filters. The subtracted bandpasses are both well-defined, and both cut on and off sharply; the extended wing of the F125LP–F140LP combination is just 5% of the integrated filter surface. The combinations F125LP–F140LP and F140LP–F150LP sample Ly α at redshifts $z = 0.028 – 0.109$ and $z = 0.134 – 0.190$, respectively, which hence defines the redshift ranges permitted by our sample selection (see Sections 2 and 3 for details). The maximal throughput of the effective bandpasses are 5 and 4% for the low- and high- z setups; for comparison the dedicated Ly α filter in SBC (F122M) has an integrated peak system throughput of 0.9%. Overlaid in blue solid and red dashed lines are STARBURST99 models of blue and red continuum spectra with Ly α lines added, and redshifted to $z = 0.04$ and 0.17 , the typical values for low- and high- z LARS galaxies (the choice made in this figure to put the blue spectrum at low- z and the red one at high- z is of course completely arbitrary). The geocoronal Ly α line, shown by the dot-dashed vertical line at 1216 Å is not transmitted by these long-pass filters.

line implies order-of-magnitude losses. To measure (or robustly constrain) all the relevant quantities complicit in Ly α transport in individual galaxies, and to simultaneously probe more detailed scales in the ISM, we need to turn to the low- z universe.

Naturally this requires large investments of time on UV-capable space-based platforms, in which field the IUE, HST, and GALEX have been pivotal. By following up various blue-compact and emission line galaxies IUE first demonstrated that radiative transport effects were most likely at play, as dust-corrected Ly α /Balmer line ratios dramatically fail to reconcile with the predictions of recombination theory (Giavalisco et al. 1996), and demonstrating the importance of gas geometry as well as direct dust attenuation. Using HST high resolution spectroscopy, Kunth et al. (1994, 1998) and Lequeux et al. (1995) first highlighted the importance of neutral gas kinematics (see also, e.g. Shapley et al. 2003a and Tapken et al. 2007 for observational results at high- z) which later enabled Tenorio-Tagle et al. (1999) and Mass-Hesse et al. (2003) to cast the Ly α emission/absorption as an evolutionary sequence following the age of the star-formation episode. However, the nature of spectroscopic observations meant that the global emission properties of the galaxies studied remained unknown, and called for the need for photometric Ly α imaging studies of local star forming galaxies.

While earlier HST cameras (WFPC, FOC, WFPC2, STIS) included Ly α imaging filters, the low integrated system throughputs ($< 0.3\%$) prevented their use for studying faint targets such as external galaxies. The arrival of ACS and its solar blind channel (SBC) resulted in a big step in far UV sensitivity and the first Ly α imaging study of six star forming galaxies in the local universe was initiated (Kunth et al. 2003). The spatial scattering of Ly α photons could be observed for the first time (Hayes

et al. 2005, 2007; Atek et al. 2008; Östlin et al. 2009). In these studies we found that when Ly α is found in emission, its luminosity is dominated by large scale, largely diffuse components. The large scale diffuse nature of the emission also means that UV spectroscopy centered of the UV-brightest parts of galaxies would miss most of the Ly α flux. This first pilot study aimed at exploring Ly α imaging of local galaxies, and while it found the first evidence for the importance of resonant scattering the small sample size and its hand picked nature prevented general conclusions and statistically significant trends to be drawn.

1.2. The Lyman Alpha Reference Sample

To remedy this situation we started, in HST cycle 18, *LARS – the Lyman-alpha Reference Sample* (GO program 12310). *LARS* is a sample of 14 star forming galaxies in the nearby universe selected from the cross-correlated GALEX General Release 2 and SDSS DR6 catalogues. In addition to Ly α , *LARS* includes HST imaging in H α , H β , optical and UV continuum, and UV spectroscopy with COS sampling Ly α and metallic lines arising in the interstellar medium of the galaxies. The UV continuum luminosity range spanned by *LARS* is similar to Ly α -emitters and LBGs at $z \sim 3$, but works at a physical resolution up to two orders of magnitude smaller than is possible at high- z . Furthermore we have obtained direct H I masses for the first time in a Ly α sample (Pardy et al., 2014 submitted to ApJ) and other crucial datasets including: far infrared spectroscopy and photometry to study dust and photodissociated gas, 3D spectroscopy for ionized gas kinematics, ground-based narrowband images in nebular lines and the continuum, and deep infrared imaging to examine the host galaxies in detail. Thus in the long term, *LARS* will provide what is easily the most extensive data set in which to study de-

tailed Ly α astrophysics. With LARS we will, in this and subsequent papers, investigate how Ly α is transported out of galaxies, what fraction of Ly α that survives, and the Ly α morphologies. We will do this as a function of physical parameters like dust and gas content, metallicity, kinematics, and stellar population properties. In order to rapidly disseminate results from the program presented here, we presented a letter (Hayes et al. 2013) showing that Ly α emission profiles in LARS galaxies typically extend over scales twice as large as those measured in the UV continuum and H α . The current paper (Paper I) presents the survey outline, sample selection and data analysis methods, plus a science demonstration for the first galaxy in the sample. In paper II (Hayes et al. 2014) we present resolved photometry of Ly α and other quantities for the full LARS sample. Subsequent paper in the series discuss integrated HI properties (Pardy et al. 2014), COS spectroscopy (Rivera-Thorsen et al. 2014 in prep), radiative transfer modeling (Orlitova et al. 2014 in prep), a detailed study of an individual target (Duval et al. 2014, in prep), comparative studies of morphologies (Guaita et al. 2014 in prep), with several more papers in preparation.

The current paper is organised as follows: In section 2 we review some observational/technical considerations that impacts the designs of the project. In section 3 we describe the sample. In section 4 we describe the HST imaging data, and in section 5 how we use these to arrive at high fidelity Ly α images. Section 6 exemplifies what can be deducted from the HST imaging and spectroscopic data by showing preliminary results for the first galaxy in the sample. Section 7 contains discussion and summary. Throughout we assume a cosmology of $(H_0, \Omega_M, \Omega_\Lambda) = (70 \text{ km s}^{-1} \text{ Mpc}^{-1}, 0.3, 0.7)$. All magnitudes given in the paper are in the AB system

2. LARS SURVEY STRATEGY AND CONTINUUM SUBTRACTION

While several possible methods exist by which Ly α can be imaged at $z \sim 0$ with HST, there are a number of important considerations regarding the available bandpasses that restrict our methods, survey strategy, and ultimately sample selection. Ly α imaging in the local universe requires access to space platforms, which in practice means HST. Whereas several HST cameras (WFPC, WFPC2, STIS, ACS) have had Ly α filters for $z \sim 0$, these have suffered from imperfect band pass shapes and low throughput. The sample of six local ($z = 0.007 - 0.029$) galaxies presented in Östlin et al. (2009) used the 'narrow' ($\Delta\lambda \sim 120\text{\AA}$ or 10%) Ly α filter (F122M) available in the solar blind channel (SBC) of ACS. This bandpass has an extended red wing, low throughput and high background since the geocoronal Ly α emission is included in the bandpass. Moreover, in order to sample the continuum, only filters at significantly (20%) longer wavelengths are available, which makes the continuum subtraction very sensitive to the spectral shape on the red side of Ly α . The Ly α EW for star forming populations has a maximum of $\sim 200\text{\AA}$ at zero age (Schaerer 2003). While diffuse regions dominated by resonantly scattered Ly α may have very high EW, the central UV bright regions have much lower values and the integrated $W(\text{Ly}\alpha)$ of local starbursts ranges

between negative (absorption) and a few 10's of \AA (Giavalisco et al. 1996; Östlin et al. 2009). Hence the Ly α line may contribute only a few percent to the flux of the F122M filter, requiring a very accurate continuum subtraction, and any attempt to just subtract the continuum using a broad filter on the red side would fail dramatically (Kunth et al. 2003; Hayes and Östlin 2006).

The near UV continuum of starbursts can in general be well characterised by a power law with index β ($f_\lambda \propto \lambda^\beta$). Hence it may seem plausible that it should be possible to continuum subtract Ly α by determining β and extrapolate the continuum to the wavelength of Ly α . However, near Ly α , the continuum evolve rapidly in wavelength with the age and dust reddening of the stellar population, and unfortunately a single UV colour is insufficient to estimate the continuum at Ly α (Hayes et al. 2005).

The solution, as shown in Hayes et al. (2005, 2009) is to estimate the continuum under Ly α through modeling the galaxy spectrum as a composite population of young stars, old stars and nebular gas. By measuring the UV spectral slope (β), the 4000 \AA break plus its fractional contributions from an old underlying stellar population and nebular gas emission, the continuum under Ly α can be accurately estimated. In practice this approach requires imaging in several band passes in addition to those capturing Ly α and its nearest continuum point.

As an alternative setup to using the dedicated Ly α filter (F122M), combinations of the ACS long-pass filters can be employed. All the long-pass filters have nearly identical long wavelength performance and the subtraction of two adjacent filters hence forms a well defined bandpass. In Fig. 1 we show the effective bandpass formed by the combination of F125LP–F140LP and F140LP–F150LP. The long pass filters have very high transmission redwards of the cut, and consequently the throughput is enhanced by a factor ~ 5 compared to the nominal Ly α filter in SBC (F122M). Furthermore, the geocoronal Ly α background, that provides the dominant source of noise in the F122M filter, is completely suppressed by using these passbands. The F125LP–F140LP bandpass combination is effective in capturing Ly α for redshifts $z = 0.028$ to 0.109 , and F140LP–F150LP for $z = 0.134 - 0.190$. While the bandpass shapes of these effective filters are much better than for F122M, the widths of these combinations are still $\sim 120 \text{ \AA}$ and since we are interested in measuring the Ly α line also in the case of low equivalent width or even absorption, the same considerations as for F122M still hold: the effective bandpasses will in many regions be strongly dominated by continuum emission. Hence, the continuum has to be modeled in the same manner but will yield more accurate results (Hayes et al. 2009).

For the starburst galaxy NGC 6090, at $z = 0.029$ (included in Östlin et al. 2009), data was available for F122M, F125LP, F140LP and F150LP prior to the submission of the LARS proposal in Cycle 18, and we could thus compare the two methods using real data. Despite the shorter exposure time in F125LP vs F122M, the signal to noise in the resulting Ly α image is increased with a factor of 7 (see appendix A.1 for further details). Given the very favorable outcome of this comparison, the combination of F125LP with F140LP was the baseline setup chosen for LARS. The higher redshift window defined by

the combination of F140LP with F150LP was expected to perform similarly well as the throughput is slightly lower, which, however, is compensated by a yet lower background. Its main drawback is the loss of physical resolution and an increased cosmological surface brightness dimming.

3. LARS SAMPLE SELECTION

Our sample selection starts out from the combined SDSS (DR6) and GALEX (DR3) data releases, which allow us to draw a UV selected sample of galaxies with known redshift. From the combined catalogs we use the redshift and Galactic reddening information from SDSS and the GALEX far UV (FUV) flux to calculate the FUV luminosity for all cross matched sources in the two possible redshift ranges (Section 2).

To ensure that our sample only contains actively star forming galaxies, i.e. galaxies that produce Ly α (whether or not it escapes), we have required a rest frame H α equivalent width of: $W(\text{H}\alpha) \geq 100 \text{ \AA}$. A galaxy with constant star formation rate still has a $W(\text{H}\alpha) > 100 \text{ \AA}$ after 1 Gyr (Leitherer et al. 1999). A lower $W(\text{H}\alpha)$ cut could hence lead to disk galaxies with slowly declining star formation dominating the sample. Indeed, we find that $W(\text{H}\alpha) \geq 100 \text{ \AA}$ leads to a sample dominated by compact ($I_{\text{FUV}} > 10^8 L_\odot/\text{kpc}^2$) systems (Heckman et al. 2005), mainly of irregular morphology, whereas for $0 < W(\text{H}\alpha) < 50 \text{ \AA}$ ordinarily looking disks seem to dominate. For an instantaneous burst with a Salpeter IMF and $Z = 0.004$ $W(\text{H}\alpha)$ drops to 100 \AA after 7 Myr. If radiative transfer effects are ignored the same population, at age 7 Myr, has $W(\text{Ly}\alpha) \approx 25 \text{ \AA}$, which is close to the rest frame limits (usually 20 \AA) for Ly α candidate selection in current high- z surveys, implying that our 100 \AA cut mostly rejects objects that could anyway not show strong Ly α . It is worth noting though that for extended star formation histories it is in principle possible to have both $W(\text{H}\alpha) < 100$ and $W(\text{Ly}\alpha) > 20 \text{ \AA}$ since the continuum dominating near H α would not contribute much near Ly α . Having a sample unbiased in $W(\text{H}\alpha)$ could in a sense have been preferable but would risk being contaminated by post starburst galaxies and given the limited sample size we have focused on galaxies with very active star formation that are likely to have intrinsically strong Ly α production¹⁶

Since LARS aims to investigate the Ly α properties of star forming galaxies we rejected objects with a strong AGN component by requiring the line width in H α to be smaller than FWHM 300 km/s (line of sight $\sigma < 130 \text{ km/s}$) and that the galaxies are classified as HII-like based on their [OIII]/H β , [NII]/H α and [SII]/H α ratios.

In selecting targets, we aimed to cover a range of FUV luminosities, from $\sim 10^9$ in monochromatic solar luminosities ($\nu L_\nu / L_\odot$), to as high as possible without including AGN dominated objects. Priority was given to low z objects since this maximizes the physical resolution, but in order to include the more FUV luminous objects we needed to sample larger volumes. In practice this is what led to the inclusion of a high- z (F140LP-F150LP) setup. In order to maximize the efficiency of

¹⁶ A follow up project, eLARS, to image 28 more galaxies was approved in Cycle 21. Here the cut is $W(\text{H}\alpha) > 40 \text{ \AA}$.

observing at FUV wavelengths, priority was furthermore given to objects with low foreground extinction in the SDSS database (see Table 1).

Because LARS needs many different observing modes (cameras, filters, spectra), observing a substantial sample can quickly become observationally expensive. In principle, the expense can be reduced by using archival data, when available, under the proviso that the selection function is not compromised. Hence we investigated which of the objects that fulfilled the selection criteria that also have archival data valuable for LARS. If the archival data was deemed sufficiently deep, such targets were then prioritized. SDSS cutout images, and the L_{FUV} , redshift, and $W(\text{H}\alpha)$ distributions of the final LARS sample are shown in Figure 2. Regarding relevant archival HST observations LARS overlaps with:

- Two galaxies from GO 11110 (PI McCandliss), the sample of which was originally selected on FUV flux and declination and have 3 orbits of SBC far UV imaging in the required filters each. These galaxies are represented in Figure 2 with red ID numbers and points. The remaining twelve galaxies from GO 11110 fail either the redshift, $W(\text{H}\alpha)$ or AGN criteria.
- Three galaxies (shown in blue in Fig. 2) from the Lyman break analog sample by Heckman (programs 10920, 11107) including COS spectroscopy and partial SBC imaging. This sample was selected on FUV luminosity and surface brightness. The remaining objects fail either the z , $W(\text{H}\alpha)$ and/or AGN criteria.
- Four galaxies (shown in green in Fig. 2) from the COS GTO programs (11522, 12027) of star forming galaxies (PI Green), having spectra covering Ly α and ISM absorption features. These galaxies have originally been selected on H α brightness and compactness (due to the 2.5'' aperture of COS) from the KISS objective prism survey (Salzer et al. 2001). The remainder of the sample fail the $W(\text{H}\alpha)$ and/or z criteria.

Thus in total, LARS could be directly optimized by the inclusion of seven objects, fulfilling our selection criteria, that have relevant data from other programs. In order to build a sufficient sample, 7 more targets were selected that do not have prior SBC or COS observations. An aspect that we considered for the final seven targets was that the total sample should have a reasonable distribution in FUV luminosity.

The total sample of 14 objects populate a UV luminosity range between $\log(L_{\text{FUV}}/L_\odot) = 9.2$ (corresponding to $SFR_{\text{FUV}} \approx 0.5 M_\odot/\text{yr}$, similar to the objects that expected to dominate re-ionization and that match future JWST goals) and 10.7 (roughly the characteristic luminosity, L_* , for LBGs, Reddy et al. 2008). The L_{FUV} range also encompasses that of the 'double blind' Ly α + H α sources at $z = 2$ (Hayes et al. 2010), high- z LAEs (e.g. Nilsson et al. 2009), GALEX selected LAEs (Deharveng et al. 2008) and the $z \sim 0.2$ GALEX selected 'LBG analogs' (Hoopes et al. 2007; Overzier et al. 2008). This implies that the results from LARS can be meaningfully compared to numerous other studies.

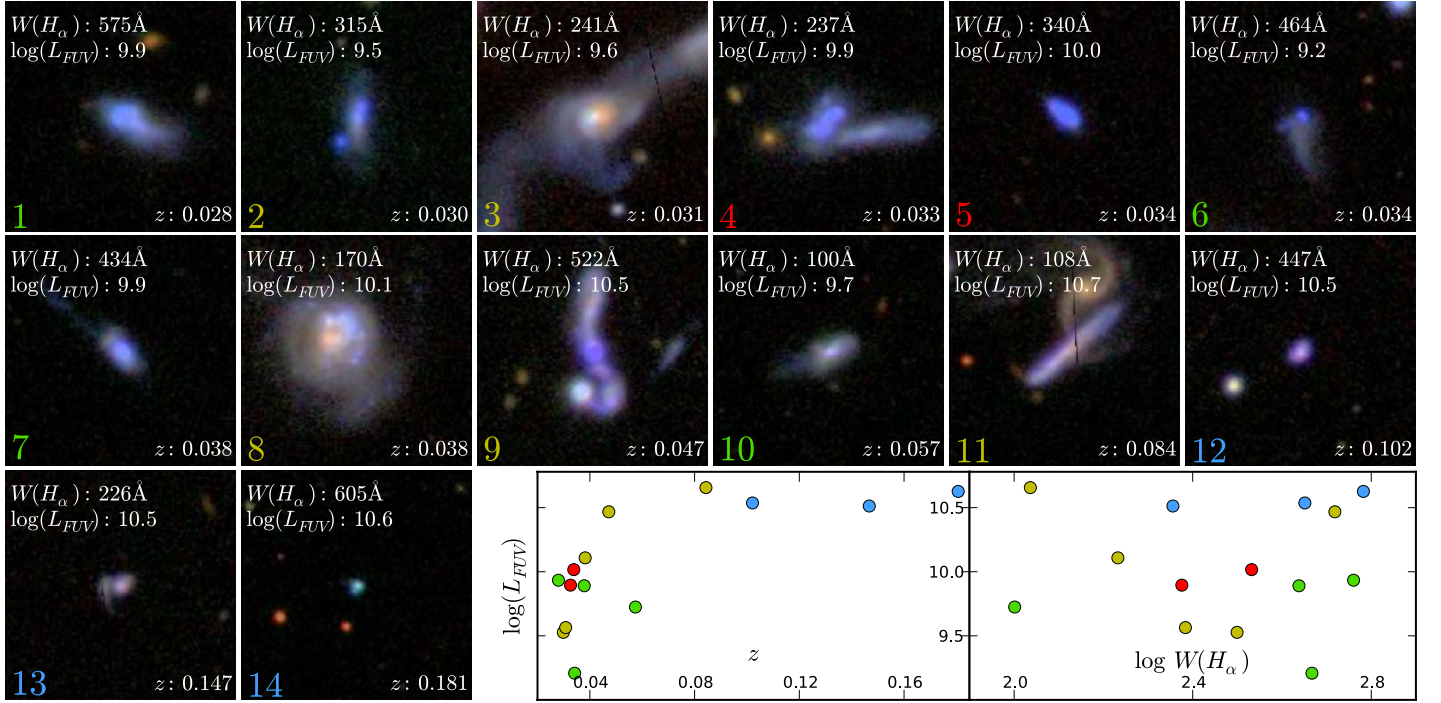


Figure 2. LARS sample as seen by SDSS, in $40'' \times 40''$ thumbnails. Each panel is numbered with its LARS id number (increasing with redshift) in the lower left corner, its redshift in the lower right corner, and the $W(H\alpha)$ and L_{FUV} values upper left. The LARS id numbers are color coded according to their selection: green (COS GTO targets), red (from McCandliss sample) and blue (Lyman Break Analogs) numbers means that the target was originally included in another sample (see text for details) while numbers are yellow for genuine LARS targets. Lower right panels show the L_{FUV} vs z and $W(H\alpha)$ distributions, where the color coding has the same meaning.

Table 1
LARS Selection

| LARS ID # (1) | SDSS object ID (2) | redshift z (3) | $W(H\alpha)$ Å (4) | m_{FUV} AB (5) | m_{NUV} AB (6) | UV slope β (7) | E_{B-V}^{MW} mag (8) | $\log(L_{FUV})$ L_\odot (9) | common name (10) |
|---------------|---------------------|----------------|--------------------|------------------|------------------|----------------------|------------------------|-------------------------------|------------------|
| 1 | J132844.05+435550.5 | 0.028 | 575 | 16.65 ± 0.03 | 16.45 ± 0.02 | -1.55 | 0.017 | 9.92 | Mrk 259 |
| 2 | J090704.88+532656.6 | 0.030 | 315 | 17.91 ± 0.02 | 17.62 ± 0.01 | -1.37 | 0.018 | 9.48 | |
| 3 | J131535.06+620728.6 | 0.031 | 241 | 17.89 ± 0.08 | 16.92 ± 0.01 | 0.17 | 0.023 | 9.52 | Arp 238 |
| 4 | J130728.45+542652.3 | 0.033 | 237 | 16.97 ± 0.04 | 16.68 ± 0.02 | -1.36 | 0.019 | 9.93 | |
| 5 | J135950.91+572622.9 | 0.034 | 340 | 16.81 ± 0.03 | 16.81 ± 0.02 | -2.01 | 0.011 | 10.01 | Mrk 1486 |
| 6 | J154544.52+441551.8 | 0.034 | 464 | 18.91 ± 0.11 | 18.58 ± 0.06 | -1.25 | 0.020 | 9.20 | KISS 2019 |
| 7 | J131603.91+292254.0 | 0.038 | 434 | 17.68 ± 0.03 | 17.03 ± 0.01 | -0.53 | 0.010 | 9.75 | IRAS 1313+2938 |
| 8 | J125013.50+073441.5 | 0.038 | 170 | 16.91 ± 0.01 | 16.37 ± 0.01 | -0.80 | 0.034 | 10.15 | |
| 9 | J082354.96+280621.6 | 0.047 | 522 | 16.59 ± 0.03 | 16.25 ± 0.02 | -1.23 | 0.032 | 10.46 | IRAS0820+2816 |
| 10 | J130141.52+292252.8 | 0.057 | 100 | 18.66 ± 0.03 | 18.29 ± 0.01 | -1.17 | 0.012 | 9.74 | Mrk 061 |
| 11 | J140347.22+062812.1 | 0.084 | 108 | 17.24 ± 0.02 | 16.80 ± 0.01 | -1.01 | 0.025 | 10.70 | |
| 12 | J093813.49+542825.1 | 0.102 | 447 | 18.06 ± 0.02 | 17.95 ± 0.01 | -1.75 | 0.018 | 10.53 | SBS 0934+547 |
| 13 | J015028.39+130858.4 | 0.147 | 226 | 19.18 ± 0.03 | 19.01 ± 0.02 | -1.61 | 0.072 | 10.60 | IRAS 0147+1254 |
| 14 | J092600.40+442736.1 | 0.181 | 605 | 19.00 ± 0.10 | 19.10 ± 0.07 | -2.22 | 0.019 | 10.69 | |

Note. — Column (1) LARS ID number (2) SDSS name (3) SDSS redshift (4) SDSS equivalent width in H_α (5-6) GALEX FUV and NUV magnitudes. GALEX bandpasses centers use the pivot wavelengths: 1524 Å and 2297 Å for the FUV and NUV channels, respectively. (7) UV continuum slope assuming standard parameterization: $\beta \propto \lambda^\beta$. Accuracy ranges from 0.01 to 0.05. (8) Foreground extinction in E_{B-V} , as reported in the SDSS database and derived from 100 μm dust emission maps. (10) FUV luminosity in logarithmic monochromatic solar luminosities, $L_{FUV} = \lambda \times L_\lambda$. The precise restframe wavelength varies from target to target and is evaluated at 1524 Å/(1 + z).

Five of the LARS galaxies have available IRAS fluxes, and follow the IRX-beta relation by Meurer et al. (1999). Indicative stellar masses and star formation rates from the SDSS added value catalogs¹⁷ (Kauffmann et al. 2003; Salim et al. 2007; Brinchmann et al. 2004) shows that these LARS galaxies lies above the SFR-Mass main sequence Elbaz et al. (2011), indicating that they are “true” starburst galaxies, which is likely to be a conse-

quence of the $W(H\alpha)$ selection of LARS.

On a cautionary note, the targets with available SBC/COS data were originally selected by others, which means that we do not have full control of the selection function. For the Green program potential targets with large angular extent are not included. The size criterium becomes less of an issue as we go out in redshift, and the Green targets do not stand out as being systematically smaller than the other LARS targets.

¹⁷ <http://www.mpa-garching.mpg.de/SDSS/DR7/#derived>

LARS01

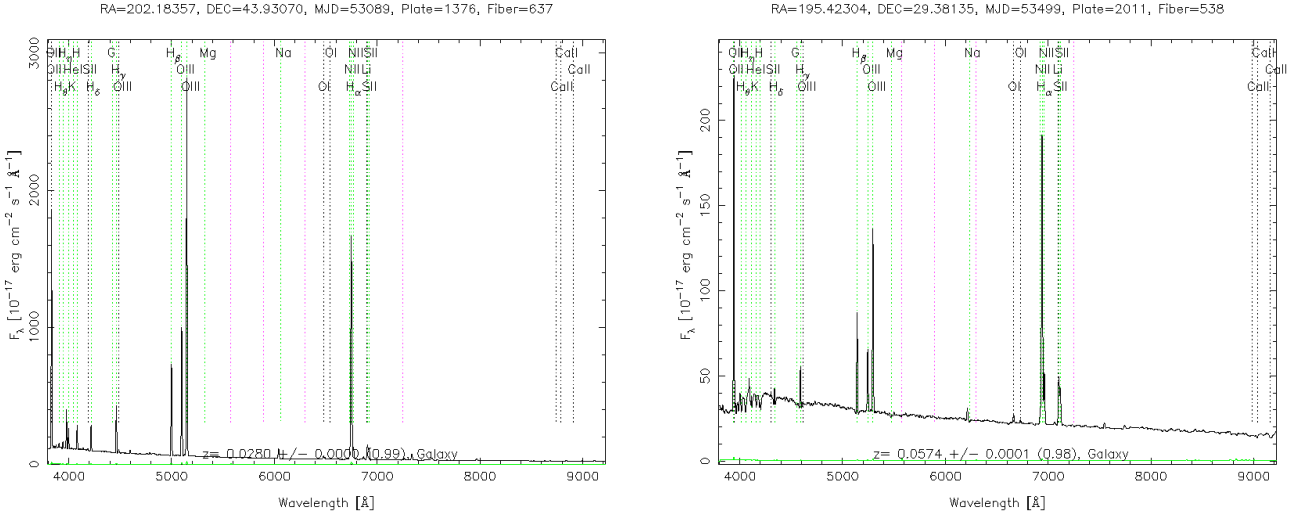


Figure 3. SDSS spectra of lars#1 and 10. LARS #1 belongs to the objects with the highest $W(\text{H}\alpha)$ according to SDSS while LARS#10 has the lowest, and therefore the most apparent contribution of an underlying stellar population.

The resulting sample of 14 galaxies and its distribution in z , L_{FUV} and $W(\text{H}\alpha)$ are presented in Fig. 2. In Table 1 we give the redshift and $W(\text{H}\alpha)$ as obtained from SDSS and ultraviolet photometric properties as measured by GALEX, and the foreground Galactic reddening. The median $E_{B-V}^{\text{MW}} = 0.019$ corresponds to 15% of the far UV photons being absorbed in the Milky Way, and only LARS #13 has a significantly higher value. Consequently, our targets also have high galactic latitudes.

We remeasured the fluxes of the most prominent emission lines in the SDSS spectra, which we present in Table 2. We use these to derive the internal $E(B - V)$, i.e. the average value within the SDSS aperture, and to estimate the Oxygen abundance of our targets. When the ‘auroral’ $[\text{OIII}]\lambda 4363 \text{ \AA}$ line is detected with sufficient accuracy (9 galaxies) we use this line to calculate O/H using the direct temperature sensitive method. When this line was not detected with sufficient S/N we used two empirical calibrations from the compilation by Yin et al. (2007). The 4363 Å line becomes weaker with increasing metallicity and the 5 LARS targets without a well detected auroral line are consequently the most metal rich in the sample, according to both of the empirical calibrations used. The values found for the Oxygen abundance range from $\sim 0.10 - 1 Z_\odot$.

The $\text{H}\alpha$ equivalent widths for the selection were taken from SDSS, obtained for a $3''$ aperture. Most targets fulfilling our selection criteria are rather compact and aperture effects will be moderate, and in any case our criteria will guarantee that any target will at least host a central active starburst. Nevertheless, with the HST images now in hand, we can recalculate the $W(\text{H}\alpha)$ (corrected for $[\text{NII}]$ assuming the values from the SDSS spectrum to hold globally). We find that $W(\text{H}\alpha)$ derived from SDSS spectra and HST images are tightly correlated. Two galaxies, LARS #10 and 11, which have the lowest $W(\text{H}\alpha)$ according to SDSS, fall below the threshold of 100 Å if measured from the reduced HST $\text{H}\alpha$ images. In Table 3 we provide the integrated $\text{H}\alpha$ equivalent widths for the full sample based on the a posteriori obtained HST $\text{H}\alpha$ images.

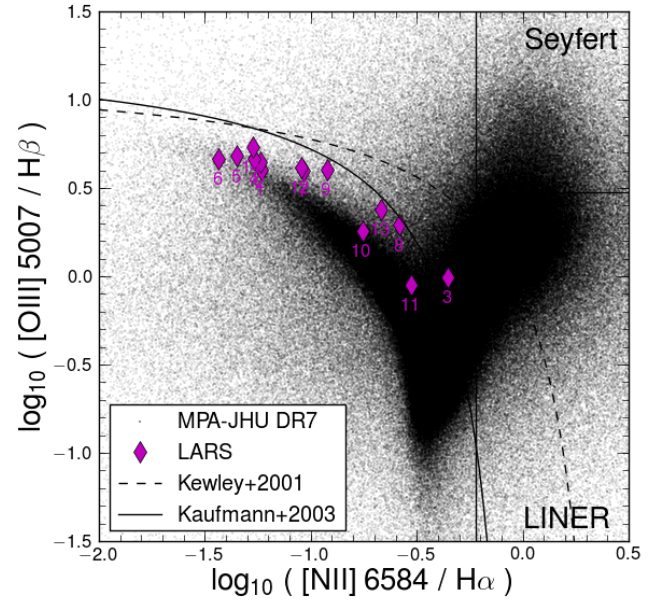


Figure 4. BPT type classification of the LARS target galaxies compared to the SDSS DR7 spectroscopic database from MPA-JHU^a and the starburst-AGN dividing lines according to Kewley (2001) and Kaufmann (2003). All targets appear dominated by star formation, with LARS#3 being rather close to the ‘Liner’ region.

^aURL: <http://www.mpa-garching.mpg.de/SDSS/DR7/>

In Fig. 3 we show the SDSS spectrum for LARS #1 which has one of the highest $W(\text{H}\alpha)$ and LARS #10 which has the lowest $W(\text{H}\alpha)$ as measured in SDSS spectra. The high $W(\text{H}\alpha)$ objects show strong Balmer and $[\text{OIII}]$ emission lines and featureless blue continua. In the lower $W(\text{H}\alpha)$ sources we see in addition underlying absorption in the higher order Balmer lines and a 4000 Å break. In Fig. 4 we show the BPT (Baldwin et al. 1981) classification for the LARS sample, indicating that they are primarily powered by star formation.

4. LARS HST IMAGING DATA

Twelve of the LARS galaxies (LARS #1 to #12) fall in the low- z window. As mentioned above, Ly α is here

Table 2
SDSS spectroscopic remeasurements for LARS sample.

| LARS ID | H α | H β | H γ | [OII]3727 | [OIII]4363 | [OIII]5007 | [NII]6584 | [SII]6717 |
|---------|---------------|-------------|-------------|---------------|--------------|---------------|---------------|-------------|
| 1 | 2070.6 ± 23.9 | 668.2 ± 7.9 | 308.8 ± 4.6 | 1512.9 ± 41.9 | 30.91 ± 0.06 | 2766.0 ± 28.3 | 117.5 ± 2.1 | 144.1 ± 2.4 |
| 2 | 396.4 ± 4.5 | 129.0 ± 1.7 | 60.8 ± 1.2 | 294.4 ± 7.9 | 7.33 ± 0.26 | 580.1 ± 5.3 | 23.0 ± 0.6 | 30.4 ± 0.7 |
| 3 | 2650.2 ± 30.7 | 444.1 ± 5.2 | 150.4 ± 2.7 | 678.0 ± 10.8 | — | 458.6 ± 5.7 | 1011.6 ± 10.5 | 319.3 ± 4.4 |
| 4 | 1146.3 ± 11.0 | 330.0 ± 4.4 | 147.4 ± 2.5 | 817.2 ± 22.5 | 15.06 ± 0.11 | 1579.4 ± 15.6 | 62.1 ± 1.3 | 80.9 ± 1.4 |
| 5 | 1173.4 ± 14.5 | 382.6 ± 4.9 | 167.5 ± 2.9 | 652.1 ± 23.7 | 39.65 ± 0.05 | 1879.4 ± 19.0 | 51.9 ± 1.3 | 60.7 ± 1.5 |
| 6 | 175.6 ± 2.2 | 59.4 ± 1.2 | 27.7 ± 0.9 | 138.4 ± 5.8 | 5.32 ± 0.23 | 274.3 ± 3.5 | 6.4 ± 0.4 | 14.3 ± 0.6 |
| 7 | 1280.3 ± 13.9 | 377.5 ± 4.7 | 158.4 ± 2.8 | 729.3 ± 22.5 | 22.65 ± 0.11 | 1554.8 ± 16.8 | 118.1 ± 2.0 | 105.2 ± 1.9 |
| 8 | 219.1 ± 2.9 | 53.6 ± 1.1 | 22.0 ± 0.9 | 140.1 ± 6.3 | — | 109.2 ± 1.8 | 57.4 ± 1.1 | 39.3 ± 0.9 |
| 9 | 1827.2 ± 17.8 | 493.4 ± 5.4 | 207.5 ± 2.9 | 798.5 ± 18.3 | 22.03 ± 0.15 | 2242.6 ± 20.4 | 199.6 ± 2.6 | 120.4 ± 1.8 |
| 10 | 225.8 ± 2.7 | 57.0 ± 1.2 | 21.0 ± 0.8 | 140.3 ± 7.7 | — | 107.6 ± 1.9 | 39.5 ± 1.0 | 37.6 ± 0.9 |
| 11 | 250.4 ± 2.7 | 55.3 ± 1.1 | 19.0 ± 0.8 | 116.3 ± 4.6 | — | 51.9 ± 1.1 | 74.6 ± 1.2 | 43.0 ± 1.0 |
| 12 | 645.0 ± 6.6 | 199.6 ± 2.5 | 84.6 ± 1.5 | 358.2 ± 23.2 | 10.26 ± 0.41 | 844.6 ± 8.4 | 58.1 ± 1.1 | 50.2 ± 1.0 |
| 13 | 277.5 ± 2.3 | 68.4 ± 1.5 | 28.5 ± 0.7 | 151.1 ± 11.8 | — | 170.5 ± 1.8 | 60.1 ± 0.8 | 32.0 ± 0.7 |
| 14 | 263.2 ± 9.1 | 76.5 ± 1.5 | 33.0 ± 1.0 | 119.4 ± 9.9 | 8.53 ± 0.78 | 418.7 ± 4.8 | 10.5 ± 0.7 | 13.2 ± 0.7 |

Note. — Line fluxes in units of 10^{-16} erg/s/cm 2 . Only [OIII]4363 measurements which were considered reliable are included.

Table 3
SDSS derived spectral properties for LARS sample

| LARS ID | z | $W(\text{H}\alpha)$ (Å) | H α /H β | [NII]/H α | E(B-V) | P | O/H T_e | O/H O_{3N2} | O/H P | $W(\text{H}\alpha)_{\text{HST}}$ (Å) |
|---------|-------|----------------------------|-----------------------|------------------|---------------|-------|-----------|---------------|---------|---|
| 1 | 0.028 | 560 ± 6 | 3.099 | 0.057 | 0.089 ± 0.015 | 0.709 | 8.070 | 8.242 | 8.241 | 400 |
| 2 | 0.030 | 326 ± 4 | 3.073 | 0.058 | 0.082 ± 0.016 | 0.725 | 8.041 | 8.226 | 8.251 | 252 |
| 3 | 0.031 | 277 ± 3 | 5.968 | 0.382 | 0.688 ± 0.015 | 0.410 | — | 8.414 | 8.915 | 208 |
| 4 | 0.033 | 580 ± 6 | 3.474 | 0.054 | 0.194 ± 0.015 | 0.721 | 8.191 | 8.191 | 8.221 | 247 |
| 5 | 0.034 | 336 ± 4 | 3.067 | 0.044 | 0.080 ± 0.016 | 0.794 | 7.800 | 8.124 | 8.135 | 442 |
| 6 | 0.034 | 529 ± 7 | 2.958 | 0.036 | 0.047 ± 0.022 | 0.726 | 7.864 | 8.082 | 8.053 | 138 |
| 7 | 0.038 | 428 ± 6 | 3.392 | 0.092 | 0.172 ± 0.015 | 0.740 | 7.911 | 8.352 | 8.447 | 366 |
| 8 | 0.038 | 186 ± 3 | 4.091 | 0.262 | 0.343 ± 0.023 | 0.511 | — | 8.505 | 8.751 | 111 |
| 9 | 0.047 | 544 ± 5 | 3.703 | 0.109 | 0.252 ± 0.013 | 0.786 | 8.051 | 8.366 | 8.519 | 265 |
| 10 | 0.057 | 105 ± 1 | 3.962 | 0.175 | 0.314 ± 0.023 | 0.506 | — | 8.505 | 8.577 | 84 |
| 11 | 0.084 | 115 ± 1 | 4.529 | 0.298 | 0.436 ± 0.021 | 0.374 | — | 8.436 | 8.807 | 77 |
| 12 | 0.102 | 445 ± 5 | 3.232 | 0.090 | 0.128 ± 0.015 | 0.760 | 8.008 | 8.342 | 8.437 | 489 |
| 13 | 0.147 | 264 ± 2 | 4.056 | 0.216 | 0.335 ± 0.022 | 0.600 | — | 8.503 | 8.669 | 204 |
| 14 | 0.181 | 700 ± 31 | 3.442 | 0.040 | 0.185 ± 0.037 | 0.824 | 7.823 | 8.055 | 8.231 | 927 |

Note. — Derived quantities from the SDSS spectra. $W(\text{H}\alpha)$ is the equivalent width of H α remeasured from the SDSS spectra. $P = [\text{OIII}]/([\text{OII}] + [\text{OIII}])$ is similar to the excitation parameter. [NII]/H α is the [NII]6584/ha value, used to correct the HST narrowband H α images for [NII] contamination, and to estimate the metallicity. O/H T_e is the oxygen abundance in units of $12 + \log(\text{O}/\text{H})$, determined with the direct method utilising the temperature sensitive [OIII]4363 line. O/H O_{3N2} is the oxygen abundance derived by the empirical O3N2 relation, and O/H P the $R_{23} - P$ relation, both from Yin et al. (2007). The last column give the integrated $W(\text{H}\alpha)$ derived from the continuum subtracted and [NII] corrected HST H α images (see Paper II, Hayes et al. 2014, for details). Note that this integrated value is in two cases smaller than the selection threshold, which was based on the value within the SDSS aperture.

captured by the F125LP and F140LP filter combination. We also include F150LP which combined with F140LP gives information on the FUV continuum slope although the spectral baseline is small. The F125LP filter omits the bright geocoronal Ly α background, but includes OI λ 1302Å and thus still has the highest background of the SBC filters. Therefore the observations in this filter were placed in the middle of the orbits when HST is in earth shadow. This dramatically reduces the airglow, and indeed, for those COS spectra of LARS targets that were obtained when HST was in earth shadow, the OI λ 1302Å line is not visible.

The additional filters required for modeling the continuum near Ly α should sample both sides of the 4000 Å break as well as longer wavelengths that are sensitive to any older underlying population. For young stellar populations, even the broad band fluxes may be dominated by

nebular line and continuum emission (Bergvall & Östlin 2002). While this can be included in the modeling, it relies on the assumption of the nebular and stellar emission being co-spatial. For a well resolved galaxy, this is often not the case as the nebular emission is often seen to be concentrated to shells and filaments. Therefore, for the current application where spatially resolved Ly α photometry is the main objective, it is clearly preferable to estimate the nebular contribution from an H α image. The Hydrogen emission lines and the nebular continuum can then be readily modeled in a way that is only (sensitively) dependent on the reddening. Other strong emission lines, notably those of [OIII], depend more on the physical parameters of the nebulae, many of which are unknown. Hence we chose the complementary broad band filters in such a way that the [OIII] lines at 4959 and 5007 Å are not transmitted, and if possible, we have also avoided the [OII] doublet at 3727 Å. The optimum

Table 4
LARS imaging exposure times (in seconds).

| bandpass alias instrument/camera spectral element | FUV-1 ACS/SBC F125LP | FUV-2 ACS/SBC F140LP | FUV-3 ACS/SBC F150LP | <i>U</i> WFC3/UVIS F336W | <i>B</i> WFC3/UVIS F438W | <i>i</i> WFC3/UVIS F775W | H β WFC3/UVIS F502N | H α WFC3/UVIS F656N |
|---|----------------------------|----------------------------|----------------------------|--------------------------------|--------------------------------|--------------------------------|---------------------------------|----------------------------------|
| LARS ID # | | | | | | | | |
| 01 | 1900 | 1807 | 1610 | 920 | 800 | 600 | 1900 | 800 |
| 02 | 2012 | 1840 | 1740 | 2000 | 1230 | 1208 | 3920 | 1265 |
| 03 | 2002 | 1984 | 1750 | 1318 | 1440 ^a | 840 ^a | 3030 | 1200 |
| 04 | 2648 ^b | 2648 ^b | 2648 ^b | 1004 | 800 | 620 | 2000 | 805 |
| 05 | 2669 ^b | 2669 ^b | 2669 ^b | 1020 | 850 | 620 | 2000 | 871 |
| 06 | 1886 | 1850 | 1650 | 1840 | 1600 | 840 | 2852 | 1600 |
| | | | | | | | ACS/WFC F502N | ACS/WFC FR656N |
| 07 | 1872 | 1806 | 1540 | 900 | 800 | 534 | 1467 | 720 |
| 08 | 1870 | 1768 | 1550 | 900 | 800 | 519 | 1452 | 720 |
| | | | | | | | FR505N | FR716N |
| 09 | 1900 | 1780 | 1538 | 900 | 800 | 534 | 1440 | 708 |
| 10 | 1872 | 1803 | 1543 | 900 | 800 | 534 | 1440 | 708 |
| | | | | | | | FR551N | FR716N |
| 11 | 1900 | 1688 | 1490 | 900 | 800 | 519 | 1457 | 720 |
| 12 | 1545 | 1300 | 2640 ^c | 1020 | 800 | 604 | 1640 | 740 |
| | | | | F390W | F475W | F850LP | FR551N | FR782N |
| 13 | — | 2711 | 2580 ^d | 900 | 800 | 519 | 1350 | 720 |
| 14 | — | 2805 | 2610 ^c | 1239 | 1098 | 2274 ^d | 2472 | 2340 ^d |

Note. — This table specifies the HST imaging observations that are used in LARS to produce Ly α images and other data products. Left column gives the LARS ID number and the other columns the exposure times (in seconds) for each filter in question. Each column is labelled with the bandpass shorthand abbreviation, the instrument/camera and spectral element used. The LARS ID number increases with redshift and hence the filters used to capture H α and H β differs as we go to higher ID numbers, as indicated. The other filters stay the same except for LARS #13 and #14 where also the *U*, *B*, *I* filters have changed. Each exposure was split in 2-4 sub exposures. Entries with superscripts come from the HST archive: *a*: Instead of WFC3 we use F435W and F814W taken with ACS/WFC under program 10592 (PI Evans); *b*: Data from program 11110 (PI McCandliss), *c*: Data from program 11107 (Heckman), *d*: Data from program 10920 (Heckman).

filter set for the low- z window is WFC3/UVIS F336W, F438W and F775W.

By also including H β imaging we can perform a Ly α continuum subtraction that is not dependent on assumptions on how the nebular reddening relates to that of the stellar population – instead, we can test how Ly α emission depends on this vital parameter. The H α and H β filters were obtained through WFC3/UVIS narrow band filters whenever one that matched the wavelength of the redshifted Hydrogen lines (while not including the [OIII] lines near H β) existed. When there was no matching conventional narrow band filter in WFC3 or ACS, we used instead the 2% wide tunable linear ramp filters (LRF) in ACS/WFC. The filters used to observe H α generally partly transmits also the adjacent [NII] lines (which we use the SDSS spectra to correct for assuming the values in Table 3 to hold globally¹⁸). In Fig. 5 we show the near-UV/optical band pass selection for LARS#1 together with the placement of strong emission lines.

For the higher redshift targets, we used F140LP and F150LP with SBC, and the near-UV/optical filters chosen were WFC3/UVIS/F390W, F475W, F850LP.

The LARS imaging (except for archival data) was ex-

ecuted between October 2010 and February 2012. All imaging observations are presented in Table 4

5. IMAGE PROCESSING AND Ly α IMAGE GENERATION

5.1. Reductions

Images were drizzled onto a common pixel scale and orientation with the MultiDrizzle tools in STScI/Pyraf. For this we adopt the 0.04 arcsec/pixel scale of WFC3/UVIS, with which most optical data was obtained and which is intermediate between ACS/SBC and ACS/WFC. Additional tweaking of the alignment between images obtained in different visits was then performed using well centred star clusters and the GEOMAP/GEOTRAN tasks in PYRAF.

Corrections for Charge Transfer Efficiency (CTE) losses in ACS were performed using the tools developed by Anderson and Bedin (ISR ACS 2010-03)¹⁹. The WFC3 camera is newer and had not suffered much radiation damage at the time when the LARS imaging was being carried out (LARS imaging begun 19 months after WFC3 was installed during SM4), hence CTE performance is better. When the first LARS imaging data processing was carried out, no CTE correction tool had been released for WFC3, but it will be included in our

¹⁸ We are in the process of acquiring ground based spatially resolved [NII]/H α maps to study the validity of this assumption and which will be used in future LARS data releases.

¹⁹ <http://www.stsci.edu/hst/acs/software/CTE>

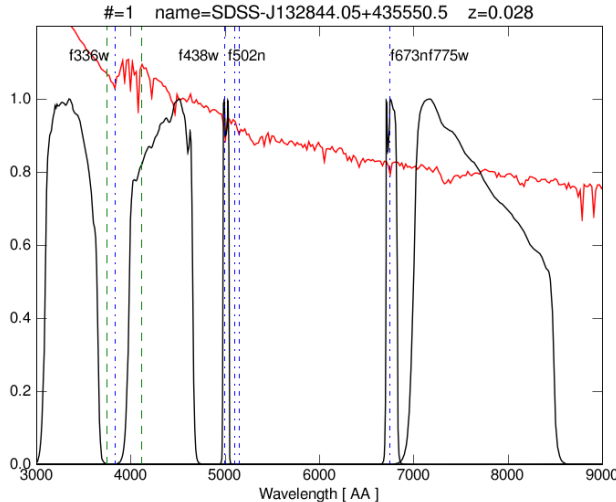


Figure 5. WFC3/UVIS filter setup used for LARS target #1, together with an arbitrary chosen SB99 model spectrum. Vertical blue dash-dot lines show redshifted wavelengths of the [OII], H β , [OIII], and H α emission lines. Vertical green dashed lines show the location of the Balmer and 4000Å breaks.

future LARS public data release.

On analyzing the HST imaging results and comparing with spectroscopy we found a small systematic difference in the flux calibration of SBC images and COS spectra which on further investigation of archival data is found to arise from the SBC zero points. We recalibrated these data by using combined SBC imaging and prism spectroscopy of the globular cluster NGC 6681, see Appendix A.2 for details.

The SBC images have very low background, especially since the F125LP observations were done in SHADOW mode when the telescope is in earth shadow. Remaining background were removed by estimating its level near the corners of the camera, far from the sources. The background in the filters obtained with ACS/WFC or WFC3/UVIS were removed in the same manner.

PSF matching: Matching of the point-spread function (PSF) was also performed. If the fraction of energy received from a point source in the central pixel varies from filter to filter we would get spurious results on small spatial scales. PSF matching is thus necessary because the Ly α extraction software uses multiple bandpasses to model the continuum near Ly α on a pixel to pixel (or spaxel) level in order to obtain a spatially resolved Ly α image. It is particularly important for matching the FUV SBC data to the optical data, since the SBC PSF shape is very different from that of ACS/WFC and WFC3/UVIS. Ordinarily this would be done by building empirical PSFs from point-sources located within the field, but the small field of view and far UV imaging observations preclude this method. As such we rely upon synthetic PSFs generated for each of our observational setups with TinyTim. We measure the FWHM of the synthetic PSF generated for each bandpass and use the broadest PSF image as the reference. We use the PYRAF/PSFMATCH task to generate the convolution kernel that will smear the PSF of each image to the best possible representation of that of the reference image.

This process is sub-optimal, and from simulations we

note a relative flux residual error in the core of objects at the 20% level. We note also that this experiment has been performed on synthetic data. For future LARS data releases we are in the process of developing an improved scheme for PSF matching such that the results can be trusted down to the individual pixel level (Melinder et al. in prep).

Voronoi tessellation: As shown by Hayes et al. (2009), reliable continuum subtraction requires a local S/N of 5 or greater. The S/N per pixel in the centre of LARS targets easily exceeds this allowing data analysis at full HST resolution (modulo the PSF matching effects). In the faint outer regions, on the other hand, the S/N per pixel may be well below one. The procedure of Voronoi tessellation – adaptive binning – enables us to maintain the spatial resolution when S/N is high, and where S/N is low aggregate pixels together to improve local S/N. For this we used the WVT binning algorithm by Diehl & Statler (2006), which is a generalization of the Voronoi binning algorithm of Cappellari & Copin (2003). We produce a binning pattern mask from the F140LP image requiring a local S/N of 10 and a maximum bin size of 625 pixels (1 square arcsec). The minimum bin size is artificially set to 4 pixels (i.e. larger than the HST PSF FWHM in any of the filters used) in order to mitigate effects of imperfect PSF matching. The binning pattern defined by the F140LP image is then applied to the other filters. Since massive star formation tends to be concentrated to the knots, while the underlying stellar distribution is distributed on larger scale, the longer wavelength broadband filters tend to have S/N larger than F140LP except in the smallest spaxels.

5.2. Continuum subtraction – LaXs, generation of Ly α images

As discussed in (Hayes et al. 2005, 2009), the production of continuum subtracted Ly α images from raw ACS/SBC data is a non-trivial process because of the broad nature of the bandpass that captures Ly α . As such, it becomes necessary to pay close attention to the behaviour of the continuum at all wavelengths sampled by F125LP filter (or F140LP for the high-z window). In order to estimate this continuum behaviour we need an accurate picture of the age of the stellar population that dominates the light output at $\lambda < 1500\text{Å}$ and the attenuation it suffers due to dust. Thus we need a spatially resolved spectral energy distribution (SED) fitting tool, and a data set that has enough wavelength sampling points across the UV continuum (sensitive to both age and dust) and the 4000Å break (particularly age sensitive) to recover these two quantities in a non-degenerate fashion. Unlike in most applications of SED fitting, our galaxies are well spatially resolved and we are able to resolve composite populations including young stars, their associated nebulae, and underlying stellar populations. These additional populations of gas and old stars will not contribute significantly to the continuum in F125LP, but they may be substantial and even dominate our observational determination of the 4000Å break (restframe $U - B$), biasing our fit. To mitigate the influence of an underlying population and nebular gas we include a longer wavelength sampling point (i band) and the direct measurement of the nebular contribution through an H α

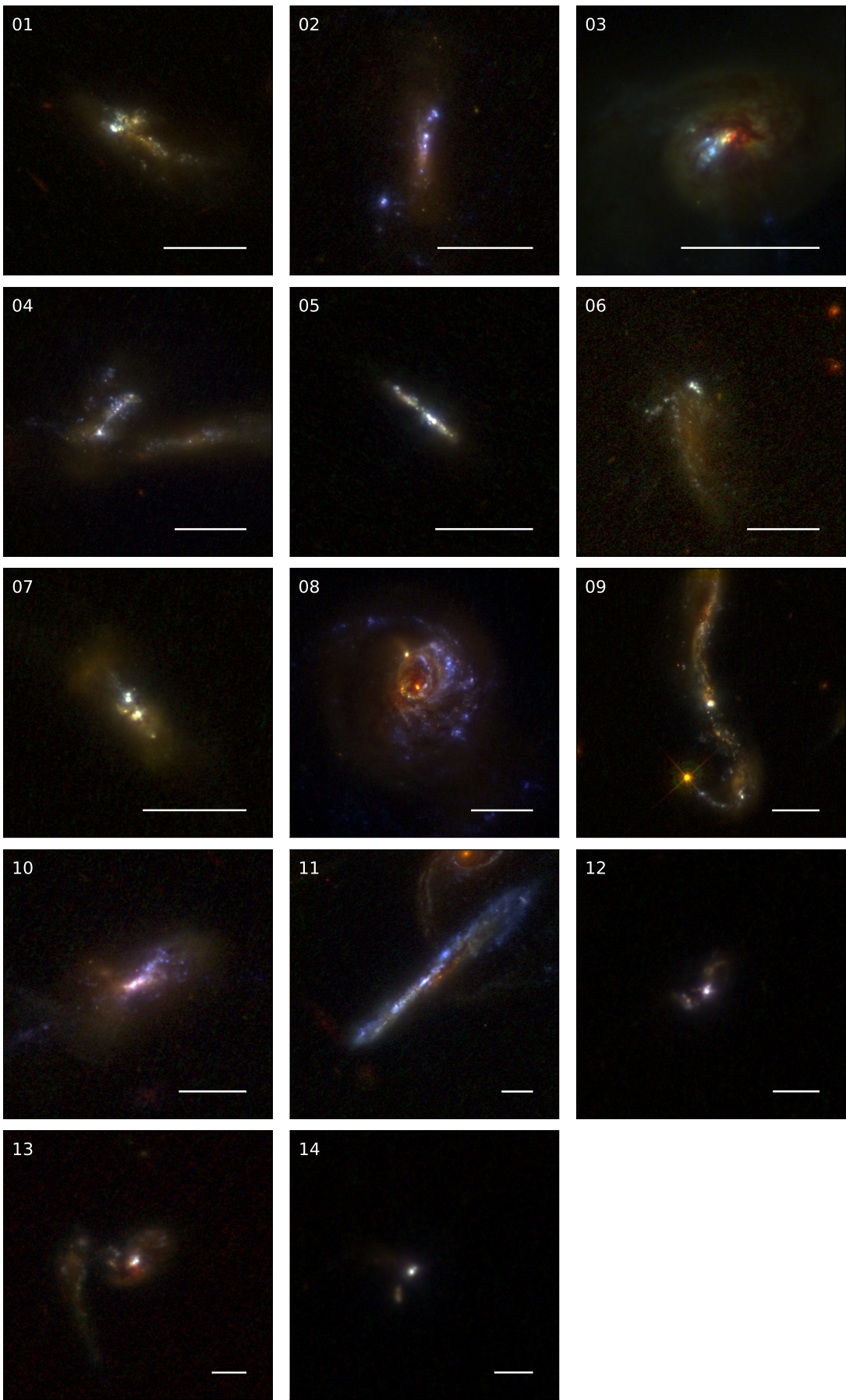


Figure 6. The full LARS sample as seen by HST. RGB composite made from FUV, *B* and *i*-band. North is up and East to the left. White bars in the lower right corner shows a constant physical size of 5 kpc.

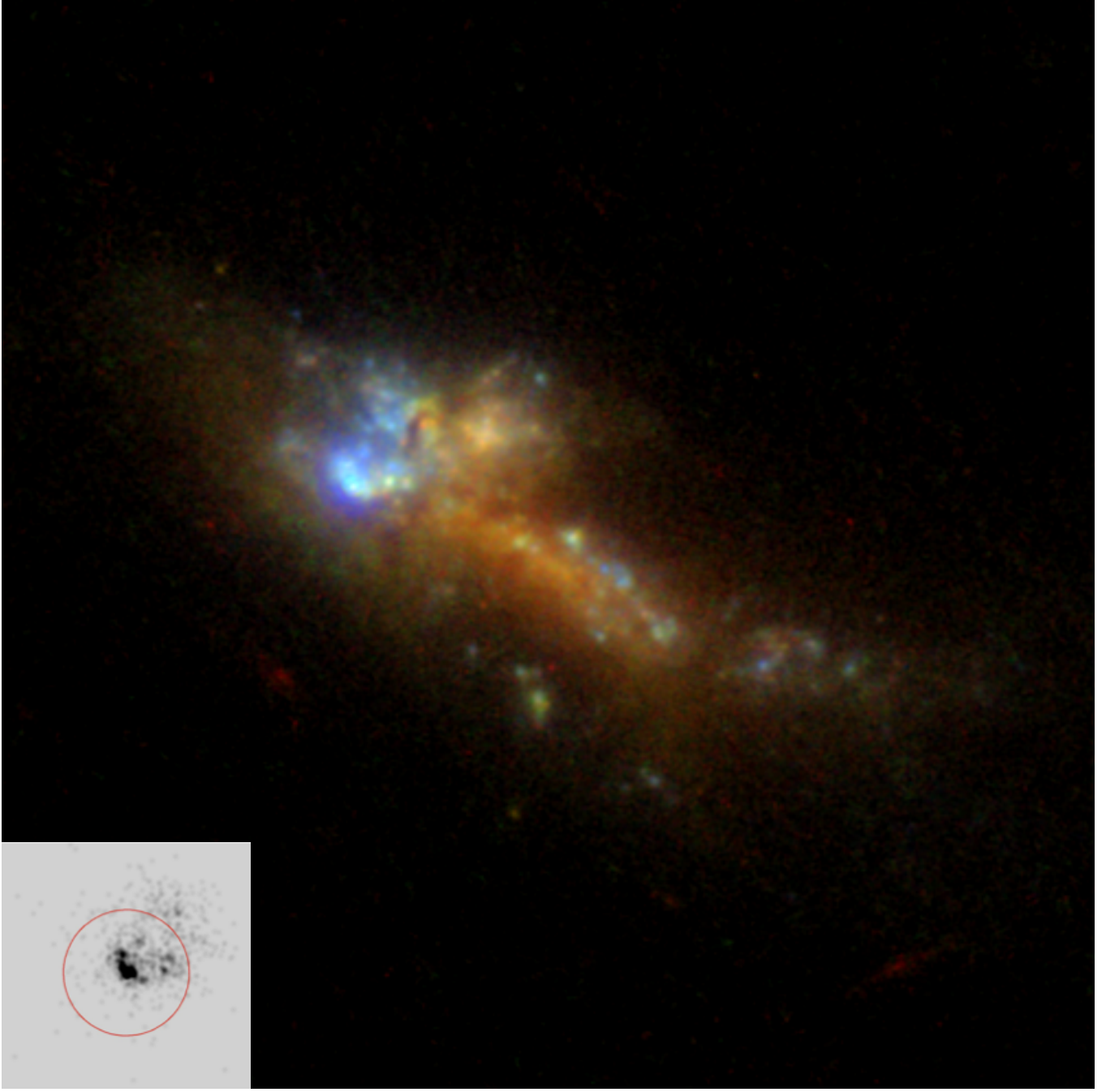


Figure 7. Mrk 259 in false color, showing the F140LP filter (FUV) as blue, F438W (*B*) as green, and F775W (*i*) as red. FOV = $21''.5 \times 21''.5$ (12 \times 12 kpc), north is up, east is left. The inset on the lower left shows the COS NUV acquisition image with the COS spectroscopy aperture (diameter $2.5''$) indicated with the red circle. The COS aperture was placed on the brightest UV (blue) knot.

image.

The continuum subtraction methodology, including composite stellar components and nebular gas is presented in Hayes et al. (2009). In short we convolve theoretical/model SEDs with the HST filter response function given by SYNPHOT (which includes any red leaks). First we generate the best possible nebular gas SED, compute its contribution to every filter and subtract it from the observed data-points. Then we perform a two component stellar SED (using one young and one old population) fit to the broadband data points. We then reconstruct the contributions of the various components

to the F125LP bandpass and subtract it from the observation, leaving us with net Ly α line fluxes, either in emission or interstellar absorption against the UV continuum.

The continuum subtraction is implemented by the *LARS eXtraction software (LaXs)*, which performs a full stellar population analysis in each pixel and reconstructs the predicted flux due to continuum processes in F125LP, and also the narrowbands that sample H α and H β . For the template libraries we use the *Starburst99* population synthesis models (Leitherer et al. 1999; Vázquez & Leitherer 2005). In Hayes et al. (2009) we showed assump-

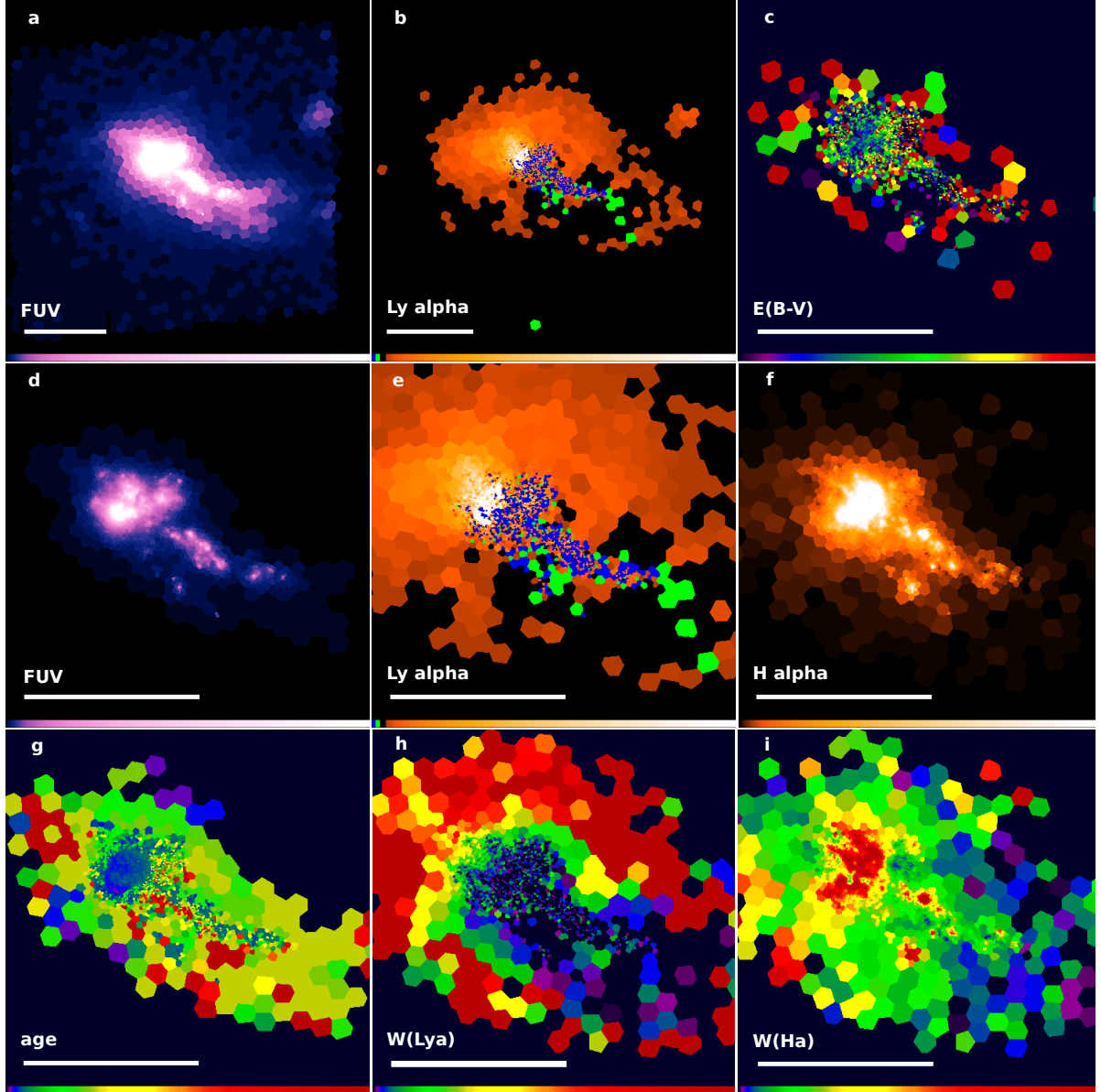


Figure 8. Voronoi tessellated images of Mk 259. For all panels the scale bar has a length of $10''$ (or 5.6 kpc) and north is up, east is left. The zero and maximum intensity limits for each panel is indicated in square brackets. Panels **a** and **b** have a size of $40'' \times 40''$ while the other panels are zoomed in to $20'' \times 20''$. **Upper left (a):** Far UV (F140LP) continuum in logarithmic intensity scaling $[0,1.25] \times 10^{-16}$ erg/s/cm 2 /arcsec 2 . **Upper middle (b):** Ly α line intensity in log scaling $[-0.2, 6.25] \times 10^{-14}$ erg/s/cm 2 /arcsec 2 . Black regions corresponds to zero, while green show (slight) and blue (more) absorption. **Upper right (c):** E(B-V) based on H α /H β in linear scale from $[0,0.5]$. **Middle left (d):** Zoom in on the far UV continuum in logarithmic scaling $[0,3] \times 10^{-16}$ erg/s/cm 2 /arcsec 2 . **Center (e):** Ly α as above but zoomed in (same intensity scale). **Middle right (f):** H α intensity in log scaling $[0,2] \times 10^{-14}$ erg/s/cm 2 /arcsec 2 . **Lower left (g):** Age of young population in log scale, $[1,60]$ Myr. **Lower middle (h):** $W(\text{Ly}\alpha)$ in log scale $[0,900]$ Å. Black regions have zero or negative $W(\text{Ly}\alpha)$. **Lower right (i):** $W(\text{H}\alpha)$ in log scale $[0,900]$ Å. For panels **c** and **g** regions fainter than $\mu_{\text{Ly}\alpha} = 25.5$ mag/ \square'' have been masked out, while for panels **h** and **i** the mask level is 26.2 mag/ \square'' .

tions about the IMF to have a negligible impact upon our ability to recover Ly α quantities, but that stellar metallicity needed to be known to within a factor of about 2. For the first generation of LARS images we assume a Salpeter IMF between the mass limits of 0.1 and $100 M_\odot$ and stellar metallicity of $Z = 0.008$. We assume that each spaxel can be approximated by an instantaneous burst (simple stellar population, i.e. characterized by just its age) together with an underlying old component. We first take the optical broadband data and perform a rapid 1-component SED fit which we use to continuum-

subtract the H α (correcting for the contribution of [NII] using the SDSS values and the filter transmission at their redshifted wavelengths) and H β narrowband observations. Since at low nebular equivalent widths these can be strongly affected by stellar absorption, we correct for this by performing a multi-component SED fit, and measure the intrinsic stellar absorption in H α and H β from the high-resolution templates (Martins et al. 2005). With the (stellar absorption corrected) H α and H β fluxes we calculate the nebular dust attenuation (parameterized by E_{B-V} assuming the SMC law Prevot et al. 1984). As

shown by Mas-Hesse & Kunth (1999) and discussed in (Hayes et al. 2005), we expect the strong UV radiation field in sources such as these to destroy the bulk of the graphite molecules, leaving a dust composition without the absorption bump at $\approx 2200\text{\AA}$.

From dust corrected H α we generate the intrinsic nebular continuum spectrum from points presented in Aller (1984), and add nebular lines according to the prescription of Anders & Fritze-v. Alvensleben (2003). The whole nebular spectrum is then reddened by the inferred E_{B-V} . Note that this is the same prescription for adding nebular emission as adopted by Schaerer & de Barros (2009, 2010), and allows us to first order to account for the effect of weak emission lines falling within our broadbands. After convolving this scaled nebular spectrum with our broadband filter profiles we subtract the gas spectrum from all our images leaving us with “true” stellar emission images. We then perform a two component stellar SED fit to the data and by the same methods, produce a map of the estimated flux due to purely continuous processes in F125LP. This is subtracted from the observation leaving us with the Ly α -only image.

The fitting procedure is based upon a brute-force minimization of the χ^2 statistic, with four free parameters; χ^2 is defined as:

$$\chi^2 = \sum_i \frac{d_{\text{stel},i} - [n_{1,i} \cdot m_{1,i}(\text{age}, E_{B-V}) + n_{2,i} \cdot m_{2,i}]}{\sigma_i^2} \quad (1)$$

where subscript i refers to the i^{th} data-point (corresponding, in the low redshift case to filters F140LP, F150LP, F336W, F439W and F775W) d_{stel} refers to the observational data-points that have had their nebular component subtracted, σ_i refers to the observational error on d_{tot} . Furthermore, n refers to the normalization and m the modeled fluxes, and subscripts 1 and 2 refer to the young and old stellar components respectively. Synthetic fluxes in the young population are a function of age, and stellar attenuation. Thus the free parameters in the fit are the normalization of the two stellar populations, and the age and dust attenuation in the young population. Since we have five datapoints included in the χ^2 fit, we have limited the number of free parameters to four in order not to overfit the problem. Therefore, the age of the old population was fixed at age of 4 Gyr and is assumed to have the same reddening as the young population. While these last two constraints are not very well motivated on scientific grounds, they have quite limited impact on the derived Ly α properties – the important aspect is that one red population should be included to account for possible underlying populations which could otherwise affect the 4000-break.

6. FIRST RESULTS FOR LARS#1 (MARKARIAN 259)

To demonstrate the potential of the LARS program, in this section we present some early results for the first and nearest galaxy in the sample: LARS#1, also known under the common name Markarian 259. Its optical appearance as seen by SDSS is shown in Figure 2 together with its SDSS spectrum in Fig. 3. Measured spectral information is summarised in Tables 2 and 3. For the assumed cosmology the scale is 573 pc/arcsec.

In the SDSS spectrum we are able to identify and

measure a number of optical emission lines relevant for studying the fundamental nebular properties of Mrk 259, which are listed in Table 3. From these lines we are able to determine a slight nebular reddening, measuring $E_{B-V}=0.089$ magnitudes based upon H α /H β . We deredden the observed line fluxes and derive an electron temperature of 12,400 K, and a nebular oxygen abundance of $12 + \log_{10}(\text{O/H}) = 8.07$. At 4817 \AA , we identify Wolf-Rayet features, redshifted from 4686 \AA implying the presence of very young stars, 2-5 Myr, see Wofford et al. (2013). The lack of a strong 4000 \AA break also points to a very young dominating cluster without any significant contribution from an evolved underlying population within the SDSS fiber aperture.

6.1. LARS images of Mkn 259

In Fig. 7 we show the appearance of LARS#1 in HST images with F336W in blue, F438W in green and F775W in red. The galaxy has an integrated absolute magnitude of $M_B = -19.2$ and possesses a highly irregular morphology, suggesting that it may have been produced in a small galaxy merger. Lots of compact star clusters are seen like in the nearer targets studied in Östlin et al. (2009) and come in different colors suggesting a spread in ages. The brightness peaks NE of the center where we see a very blue UV bright region. The geometrical centre is redder containing many dust absorption features.

In Fig. 8 we show some of the LaXs output results for LARS#1. Each sub panel shows the scale with a white 10'' long bar. In the upper left panel (a) we show the FUV image, where the Voronoi tessellation pattern is obvious in the outskirts of the galaxy. In the upper central panel (b) we show the resulting Ly α image in the same spatial scale: emission is coded in red to white, black shows close to zero emission, while spaxels where Ly α is in absorption is shown in green and blue. Obviously, the asymmetry seen in the UV/optical is even more pronounced in Ly α . The Ly α brightness peak roughly coincides with the UV brightest region (although this region also presents significant Ly α absorption). However, most of the Ly α emerges from NE of this, whereas the SW region is much fainter and contains lots of Ly α absorption regions.

The remaining panels have all been zoomed with a factor of two. The mid-left (d) and mid-central (e) panels show the same images as above, but now with more detail. In the remaining panels, we show $E(B-V)$, H α intensity (f), the fitted age of the young population (g), and the equivalent widths of Ly α (h) and H α (i). The intensity scales have been set to enhance detail.

The UV bright complex is the very youngest in the galaxy, consistent with the detection of WR features as discussed above and also coincides with the peak H α brightness. Towards the SW, the stellar population is older, except for some young star clusters (which appear in blue in Fig. 7), and we see the Ly α map varying between emission and absorption on small scales, with the equivalent width ranging between approximately -40 and $+40\text{\AA}$ (see panel h). We interpret this as some sight-lines having a smaller covering fraction of static HI which could be due to the ISM being porous, and/or small scale velocity structure. Some regions which have a high $W(\text{H}\alpha)$, e.g. star clusters in the SW tail, show

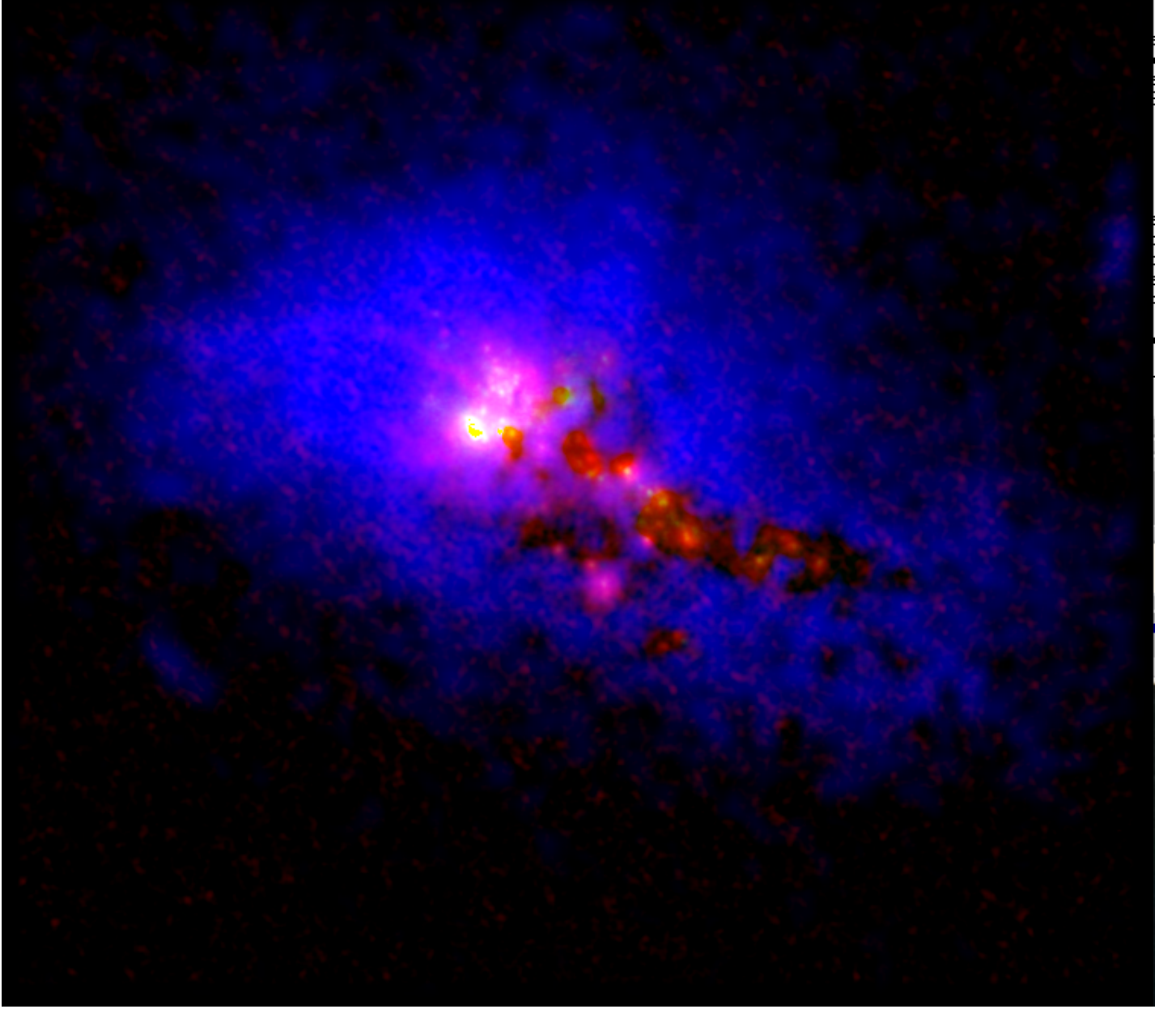


Figure 9. Mrk 259 in false color with arcsinh intensity scaling and cuts levels set to show diffuse Ly α . H α is shown in red, FUV continuum in green and Ly α in blue. The Ly α image is based on the non-binned output from LaXs and has been adaptively smoothed to suppress noise on large scales while preserving small scale detail. FOV= $30''.4 \times 26''.8$ (17×15 kpc)

Ly α in absorption or weak emission.

Even if the central UV-bright knot also contains the pixels with the highest Ly α brightness, this region has moderate $W(\text{Ly}\alpha)(10\text{--}30\text{ \AA})$ or Ly α in absorption. The highest $W(\text{Ly}\alpha)$ is found in an asymmetric halo to the NW, with values ($\gtrsim 500\text{\AA}$), much higher than model predictions for young stellar populations. In the same regions, $W(\text{H}\alpha)$ is moderate ($\sim 10\text{\AA}$). This indicates that the NE Ly α halo originates in resonantly scattering photons produced in the UV and H α high surface brightness regions. $E(B - V)$ appears patchy with no obvious correlation with the strength of Ly α . The same can be said about the age map which, while anti-correlated with $W(\text{H}\alpha)$ as expected, gives no or little guidance about $W(\text{Ly}\alpha)$.

In Fig. 9 we show an RGB composite with the H α

line image in red, the F140LP image in green, and Ly α in blue. Here we present, for aesthetic reasons, results from running LaXs with non tessellated images; instead, the Ly α image has been adaptively smoothed (using the MIDAS task FILTER/ADAPTIV) to suppress noise in low surface brightness regions. This image now clearly shows the relative distribution of Ly α with respect to FUV and H α emission and demonstrates the spatial decoupling of Ly α from the far UV sources that ionized the gas in the first place and the original recombination sites probed by the H α image. It is furthermore obvious that the young star forming complexes that stretch out from the center towards SW (see Fig. 7) and which are bright in H α do not result in strong Ly α emission.

6.2. Surface photometry

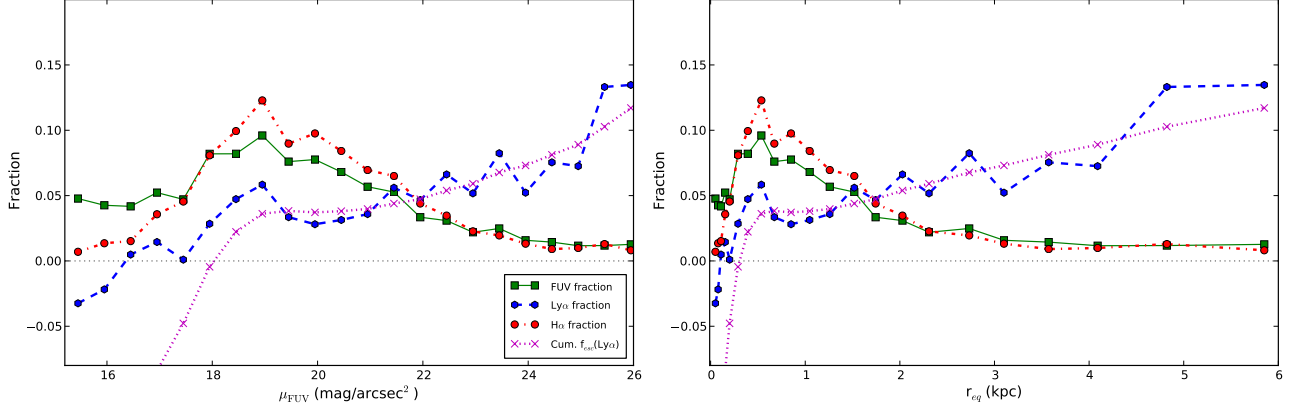


Figure 10. Escape fraction and spatial distribution of Ly α , H α , and FUV continuum. The *left* panel shows the relative flux distribution of Ly α , H α , and FUV continuum in Mrk 259 as a function of FUV surface brightness (AB magnitude per arcsec 2) as in Östlin et al. (2009). The green squares show the fraction of the total UV flux contained in each half magnitude bin ranging from $\mu_{\text{FUV}} = 15.2$ to 26.2 AB mag/arcsec 2 . The red circles similarly show how the H α flux is distributed in regions with different μ_{FUV} and the blue circles show the same for Ly α . The magenta crosses show the cumulative escape fraction obtained when integrating summing over all brighter UV resolution elements. In the *right* plot we show the same quantities but as a function of equivalent radius ($r_{\text{eq}} = \sqrt{\text{area}/\pi}$ of the isophotal areas used in the *left* panel).

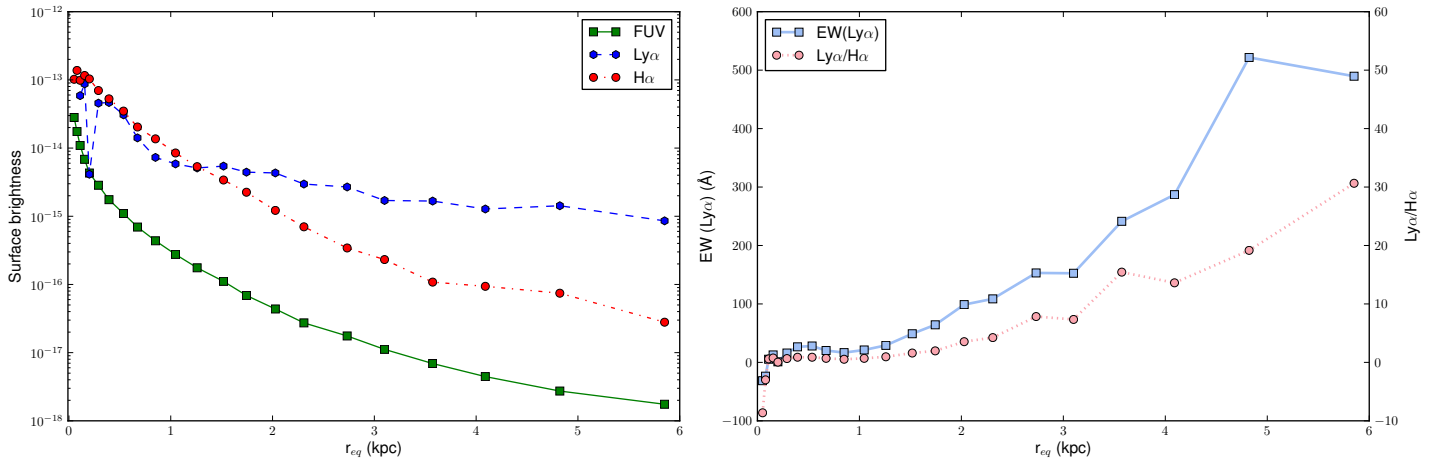


Figure 11. The *left* panel shows the surface brightness distribution of Mrk 259 obtained by isophotal integration. Green shows logarithm of the FUV continuum (in units of erg/s/cm 2 /Å), while red and blue shows the logarithm of H α and Ly α respectively (both in erg/s/cm 2). The entire FUV profile is very well fitted by Sersic profile with $n = 4$ and H α with $n = 2$. Except for the inner parts Ly α has an exponential behavior ($n = 1$). In the *right* panel, the blue squares shows $W(\text{Ly}\alpha)$ as a function of radius, while the red circles shows Ly α /H α as a function of radius.

Further insights can be obtained by comparing the radial distribution of Ly α compared to H α and FUV, which we do in Fig. 10. The left panel shows the fraction of Ly α , H α , and FUV luminosity emitted as a function of UV surface brightness integrated in 0.5 magnitude bins down to $\mu_{\text{FUV}} = 26.2$ AB magnitudes per square arcsecond, which is the limit at which the Ly α image is judged reliable. All quantities add up to unity when summed over all surface brightness bins. It can be seen that H α follows the FUV continuum relatively closely whereas the bulk of the Ly α emission comes out at lower UV surface brightness. Most of the FUV and H α luminosity comes from regions with $\mu_{\text{FUV}} = 18$ to 21 mag/ \square'' . The lower fraction of H α emission (compared to FUV) from the highest surface brightness bins may be a natural consequence of Strömgren spheres being larger than the ionising sources. For Ly α the situation is again different: the brightest UV regions show net Ly α absorption, and more than half of the cumulative Ly α emission emerges

from regions with $\mu_{\text{FUV}} \geq 22$ mag/ \square'' .

The right panel of Fig. 10 shows the same quantities as a function of FUV isophotal equivalent radius ($r_{\text{eq}} = \sqrt{\text{Area}/\pi}$). Most of the FUV and H α emission emerges from inside $r_{\text{eq}} = 1.5$ kpc and most of the Ly α comes out outside of this radius. For FUV and H α the contribution to the total flux decreases monotonically outside 0.5 kpc, while for Ly α the flux increases monotonically outside 0.7 kpc. This result can most easily be understood in terms of resonant scattering of Ly α and that the photons we detect have travelled far from their production sites. The latter should be best represented by H α . The H α half light radius is 1.2 kpc whereas that for Ly α is 4.8 kpc., and neglecting extinction effects this indicates an average total transverse scattering length of 3.6 kpc. While we conservatively only integrated the profiles out to $\mu_{\text{FUV}} = 26.2$ mag/ \square'' (after which the Ly α map breaks up into individual spaxels and noncontiguous

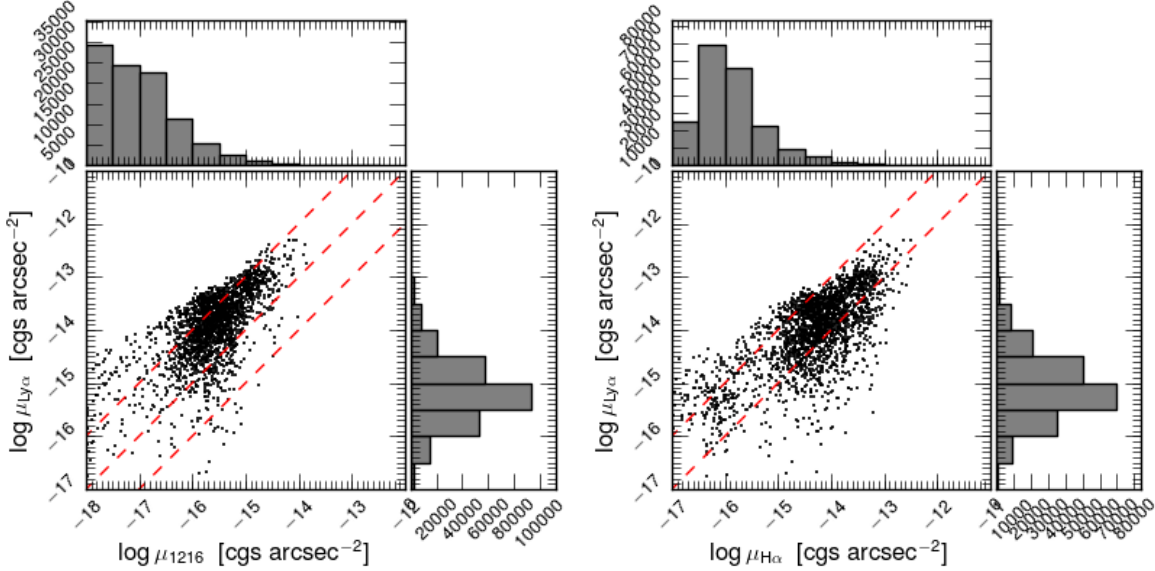


Figure 12. Scatterplots showing the surface brightness in Ly α , FUV and H α of individual spaxels. The units are erg/s/cm $^2/\square''$ for Ly α and H α , and erg/s/cm $^2/\text{\AA}\square''$ for the FUV continuum. The *left* plot shows Ly α vs FUV and the dashed lines correspond to constant values of $W(\text{Ly}\alpha)$: 1, 10 and 100 \AA . The *right* plot shows Ly α vs H α where the lower line correspond to Ly α = H α and the upper line to Ly α =9H α , i.e. the theoretical prediction from case B recombination and no reddening. The spaxels represent different areas, and in FUV faint areas they are made from summing up to 625 pixels - the histograms show the number of pixels at each brightness level. Note that since these plots show logarithmic quantities, only spaxels with positive flux are included.

areas, indicating that we have reached the background noise limit for the chosen maximum spaxel size of 1 \square'') the Ly α flux contribution is still increasing at the corresponding radius indicating that the Ly α halo may be considerably larger. At the smallest radii, the average Ly α flux is negative, suggesting a combination of dust absorption of Ly α photons and that some photons may have scattered out of the aperture.

In both panels, the cumulative Ly α escape fraction is shown by a magenta dotted line. The escape fraction was calculated as:

$$f_{\text{esc}}^{\text{Ly}\alpha} = \frac{F_{\text{Ly}\alpha}^{\text{obs}}}{F_{\text{Ly}\alpha}^{\text{int}}} = \frac{F_{\text{Ly}\alpha}^{\text{obs}}}{8.7 \times F_{\text{H}\alpha}^{\text{int}}} = \frac{F_{\text{Ly}\alpha}^{\text{obs}}}{8.7 \times F_{\text{H}\alpha}^{\text{obs}} \times 10^{0.4 \cdot E_{B-V} \cdot k_{6563}} \quad (2)}$$

where the factor 8.7 derives from the intrinsic Ly α /H α line ratio for case B (Hummer & Storey 1987) and the superscripts 'obs' and 'int' refer to observed and intrinsic quantities, respectively. At high UV surface brightness/small radius, the net Ly α output is negative, but the escape fraction increases monotonically and reaches above 10% at the limit to which we can trace Ly α at $\mu_{\text{FUV}} = 26.2$ or $r \approx 6\text{kpc}$.

Figure 11 shows the surface brightness profiles of FUV, H α and Ly α , which has again been calculated as a function of the FUV equivalent isophotal radius ($\sqrt{\text{Area}/\pi}$). The FUV luminosity profile closely follows a Sersic profile with index $n = 4$. The morphology of LARS#1 is strongly irregular, suggestive of a merger origin, and the finding that its young stars follow an $r^{1/4}$ law is consistent with observations of merger remnants like NGC 7252 (Schweizer 1982). The H α profile is more extended and best fit by $n \approx 2$ and for Ly α the profile outside $r > 1\text{kpc}$ is approximately exponential, i.e. $n \approx 1$. The neutral gas distribution of late type galaxies is usually exponential (Bigiel & Blitz 2012) and if resonant scattering by HI is the dominant mode by which Ly α is transported

through a galaxy, we expect the Ly α brightness distribution to depend on the HI distribution. As H α traces both young stars and gas we may consequently expect an intermediate behaviour. The right panel of Fig. 11 shows the radial behavior of $W(\text{Ly}\alpha)$ and the Ly α /H α ratio: for $r > 3\text{kpc}$ $W(\text{Ly}\alpha)$ exceeds the maximum predictions for young stellar populations and Ly α /H α exceeds the recombination ratio, again indicative of resonant scattering (see also Atek et al. 2008; Östlin et al. 2009)

We can also study the surface photometry of FUV, H α and Ly α on in a spatially resolved manner, i.e. on the individual spaxel level (the area of a spaxel ranges from 4 to 625 pixels, or from $0.0016\square'' = 560 \text{ pc}^2$ to $1\square'' = 0.36 \text{ kpc}^2$), which is what we show in 12. Each Voronoi-binned spaxel is represented by a point, while the histograms take the total number of contributing pixels into account. Since these are logarithmic plots, we only show spaxels that show Ly α in emission. The left panel shows Ly α vs FUV surface brightness together with lines of constant $W(\text{Ly}\alpha)$ shown in red. In the UV bright regions, pixels which have net Ly α emission shows $W(\text{Ly}\alpha)$ ranging between a few and 100 \AA . As we approach fainter continuum levels the scatter increases and notably a tail of spaxels with $W(\text{Ly}\alpha) \approx 1000 \text{\AA}$ develops. Such high $W(\text{Ly}\alpha)$ values cannot be produced by normal stellar populations. In the right hand panel we show Ly α vs H α . Similarly, at bright levels, Ly α /H α -ratios for most spaxels range between 1 and 10 in accordance with the simplest theoretical picture. In the faint tail however, line ratios up to 100 are observed.

All results presented in this section indicates that the Ly α morphology of LARS#1 is formed by resonant scattering. Moreover, the Ly α emission is markedly asymmetric with most of the emission coming out in the NE half of the galaxy. This could possibly be caused by an outflow of which the Ly α image is reminiscent. In the

central region we see Ly α changing from emission to absorption on small scales. The 'tail' has many young star clusters/HII-regions from which we detect no direct Ly α indicating a high covering fraction of static HI.

6.2.1. Global quantities

Here we summarize the total photometric quantities for Mrk 259, derived in an aperture as large as possible while still being able to trust the ingredient photometry as well as the LaXs output. For $\mu_{\text{FUV}} \geq 26.5 \text{mag}/\square''$ Mrk 259 starts to blend with the background noise, i.e. the outer isophotes start to break up and we find isolated spaxels outside the outermost connected isophote. We therefore conservatively take as our grand total the quantities achieved when integrating over areas with $\mu_{\text{FUV}} \leq 26.2 \text{mag}/\square''$.

The integrated Ly α flux we find is then $f_{\text{Ly}\alpha} = 6.95 \times 10^{-13} \text{ erg/s/cm}^2$ which translates into $L_{\text{Ly}\alpha} = 1.3 \times 10^{42} \text{ erg/s}$. For the same area, the integrated $W(\text{Ly}\alpha)$ is 44.7 \AA . For H α we find $L_{\text{H}\alpha} = 6.7 \times 10^{41} \text{ erg/s}$, and hence $\text{Ly}\alpha/\text{H}\alpha = 1.86$. Correcting H α for the extinction map that LaXs produce from H α /H β we derive $f_{\text{esc}}^{\text{Ly}\alpha} = 12.3\%$. If instead H α is corrected for the extinction derived from LaXs fit to the young stellar SED we find 19.3% (since H β measurements are rare at high z the escape fraction is normally computed from SED based reddening estimates, if considered at all). Such a high a escape fraction is rarely found at low redshift (although LARS contains 3 galaxies with even higher values, Hayes et al. 2014, paper II) but is close to the best estimate of the cosmic average at $z = 4.5$ (Hayes et al. 2011). The star formation rate inferred for H α before dust correction is $5.3 M_{\odot}/\text{yr}$, and $9.2 M_{\odot}/\text{yr}$ after dust correction using the SFR calibration by Kennicutt (1998). The integrated FUV luminosity is $L_{\text{FUV}} = 2.7 \times 10^{40} \text{ erg/s}$, corresponding to $M_{\text{FUV}} = -19.2$ (AB) and $\log(L_{\text{FUV}}/L_{\odot}) = 10.03$. Hence, Mrk 259 is detectable in deep Lyman Break Galaxy surveys up to $z = 10$ (Bouwens et al. 2014) and deep high- z Ly α surveys (Hayes et al. 2010).

Homogeneously derived global quantities for all LARS galaxies, based on the version 1 data release, are given in paper II (Hayes et al. 2014). Our values presented for Mrk 259 above are similar to those presented in paper II. The difference comes from the current paper using isophotal integration, guided by the FUV isophotes, whereas paper II used circular apertures and a smaller equivalent radius (4 kpc compared to 6 kpc in the present paper).

6.3. Hubble Space Telescope Spectroscopy

Spectroscopic observations of Mrk 259 from the COS guaranteed time program (GO 11522; P.I. Green), have been obtained from the Mikulski Archive for Space Telescopes (MAST). The G130M grating was used, providing spectral coverage between 1150 and 1450 \AA , with nominal spectral resolution of around 15 km/s near Ly α . This spectrum has also been discussed in Wofford et al. (2013). The 2.5" diameter entrance aperture of the COS spectrograph is shown together with the COS NUV acquisition image as an inset in Fig. 7.

In order to estimate the true spectral resolution we take the F140LP image and collapse and measure the one dimensional half-light radius, in the dispersion direction.

We obtain a value of 0.48'', which can be expected to reduce the spectral resolution by a factor of about 2.5, giving us a continuum resolution of about 37 km/s. In the Ly α line the degrading of spectral resolution may be more pronounced due to the diffuse nature of Ly α emission (see Figures 8 and 7, as well as Hayes et al. 2013 and Paper II). In the case that the Ly α surface brightness profile is completely flat and fills the COS aperture, we would expect $R \approx 1500$. From the analysis presented in the previous section, we find the Ly α half light radius within the COS aperture to be $\approx 1''$ indicating an effective resolution for Ly α emission of $R \approx 2250$ or ~ 130 km/s.

The spectra obtained from MAST were pipeline-processed using CALCOS, in which the main potential source of error is the adoption of correct physical coordinates for wavelength calibration. We first examine the two dimensional COS/NUV acquisition image. The inset in Fig. 7 displays the COS acquisition image, with the 2.5" primary science aperture (PSA) overlaid. The adopted centroid coordinates obtained during the acquisition procedure differ from the peak of the light distribution by just 2 pixels, corresponding to a negligible error in wavelength. Similar conclusions are reached by measuring the wavelength of the wings of the geocoronal Ly α emission.

The CALCOS output include a large number of potential error sources, which are binary-encoded in the data tables for every extracted pixel. We re-sample extracted one dimensional spectra onto a common wavelength grid and combine them, using a conservative rejection scheme that rejects every element of questionable quality, regardless of the reason; this does result in a small number of un-sampled regions in the final spectrum, but these do not fall in any of features of interest. The error spectrum is added in quadrature using the same rejection scheme.

The resulting spectrum in the regions of Ly α and selected ISM absorption features are shown in Fig. 13. The Ly α line presents a redshift of ≈ 100 km/s as measured by the difference between the Ly α peak flux and the H α velocity measured in the SDSS spectrum. The low ionisation stage (LIS) ISM absorption lines, mainly from SiII are blueshifted by a similar amount. The blueshifted ISM lines indicates the presence of outflowing neutral gas with a mean velocity of 100 km/s (see Rivera-Thorsen et al. 2014 in prep for a full analysis). This value is similar to what has been found in high- z Ly α emitters (e.g. Hashimoto et al. 2013).

A χ^2 fit to the COS UV spectrum, using the high resolution library of SB99 for the same input parameters as those adopted for the imaging results produced by LaXs give an age of 4.04 Myr, and a stellar reddening of $E(B-V) = 0.02$. Adopting a lower metallicity ($Z = 0.001$ or 0.004) give comparably good fits, and nearly identical results, while those for higher metallicity ($Z=0.02$) are worse. If instead assuming a constant star formation rate, we find an age of 24 Myr and a reddening of $E(B-V) = 0.04$. From the imaging data we derive a young population age of 4.34 Myr, and zero reddening of the stellar component, from a matched circular aperture. Hence the imaging SED fit produced by LaXs and the SED-fit to the COS spectrum produce consistent results.

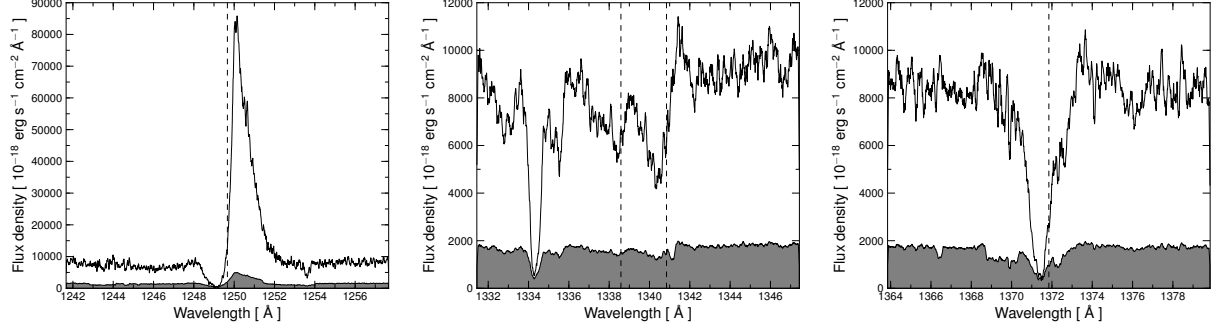


Figure 13. COS spectra of Mrk 259. On the **left** the region around Ly α is shown: the line shows a characteristic P-Cygni shape. The **middle** plot shows the spectrum around the redshifted interstellar OI λ 1302 and the **right** panel shows CII λ 1334. In all panels, the vertical dashed line shows the central wavelength each line would have if they had the same redshift as H α . The grey shaded area shows the uncertainty. The Ly α line peak is redshifted with ~ 100 km/s. The ISM lines are on the contrary systematically blue shifted and indicates the presence of outflows along the line of sight.

6.4. Lyman-alpha radiative transfer modeling

The Ly α line of Mrk 259 has a P-Cygni profile, with the observed equivalent width $W(\text{Ly}\alpha) = 9 \pm 2$ Å. A difficulty in deriving the spectroscopic equivalent width is the continuum which possesses lots of features around Ly α . From the HST imaging we derived $W(\text{Ly}\alpha) \approx 14$ Å for the area corresponding to the COS aperture. Given the very different spectral baselines of imaging and spectroscopy these numbers are quite consistent. The Ly α absorption minimum is located at ~ -130 km/s, approximately at the mean outflow velocity as measured by the ISM absorption lines (Rivera-Thorsen et al. 2014 in prep). The main Ly α peak is located at $\sim +110$ km/s. However, as discussed in Mas-Hesse et al. (2003), this value is highly dependent on the spectral resolution. This is an effect of the convolution of the sharp, steep blue edge profile produced by scattering, and the instrumental profile. Our measurement differs from that of Wofford et al. (2013), due to the revised systemic redshift, which we derived from our custom-made fits to the SDSS emission lines. A weak blue peak is present at ~ -400 km/s. The red Ly α peak has a visible substructure at $\sim +230$ km/s, and weaker ones at $\sim +300$ and $\sim +390$ km/s. In the homogeneous shell model, these should ideally be multiples of the outflow velocity.

The observed Ly α line profile thus encodes the information about the neutral gas and dust in which the Ly α photons diffuse. Radiative transfer models provide keys to decoding the ISM parameters, which is essential for the high-redshift galaxies where other data are scarce. LARS as a low-redshift sample, on the other hand, provides an opportunity for detailed checking of the Ly α model predictions and independent, multiwavelength data.

We use the enhanced version of the *MCLya* 3D Monte Carlo radiation transfer code of Verhamme et al. (2006), which computes the detailed physics of the Ly α line and the adjacent UV continuum, for an arbitrary 3D geometry and velocity field.

We here assume the geometry of an expanding, homogeneous, spherical shell of neutral ISM (H i and dust, uniformly mixed), which surrounds the starburst producing UV continuum and Ly α emission in HII regions. This geometry is an approximation of the outflows which seem ubiquitous in starburst galaxies (Shapley et al. 2003b), and it has been successful at reproducing the Ly α line

profiles of low- and high- z galaxies (Verhamme et al. 2008b; Schaerer & Verhamme 2008; Dessauges-Zavadsky et al. 2010; Vanzella et al. 2010; Lidman et al. 2012; Leitherer et al. 2013). The shell is characterised by four parameters: the radial expansion velocity v_{exp} , the H i column density N_{HI} , the H i Doppler parameter b , and the dust absorption optical depth τ_a . For each parameter set, a full Monte Carlo simulation was run, constructing a library of > 6000 synthetic models (Schaerer et al. 2011). We assume the intrinsic spectrum to be composed of a flat stellar continuum and a Gaussian Ly α line, characterised by a variable full width at half maximum $FWHM(\text{Ly}\alpha)_0$, and equivalent width $W(\text{Ly}\alpha)_0$. The theoretical spectra were smeared to the observed spectral resolution derived from the Ly α source extent (Sect. 6.3).

We used an automated line profile fitting tool exploring the full parameter space of the model grid, as described in Schaerer et al. (2011): $0 < v_{\text{exp}} < 700$ km/s; $10^{16} < N_{\text{HI}} < 10^{22}$ cm $^{-2}$; $0 < \tau_a < 4$; $10 < b < 160$ km/s. The intrinsic Ly α equivalent width was varied between 0 and 300 Å, and the FWHM between 0 and 300 km/s.

6.4.1. Results of the Ly α model fitting

The best-fitting model of the Ly α profile, from the simple shell model is presented in Fig. 14. It reproduces the overall spectral shape, the position and shape of the main peak (including some of the red-wing substructure), the position, depth and width of the absorption trough, and the presence of a weak blue peak (whose amplitude is underestimated by the model, though). The best-fit solution is characterised by: $v_{\text{exp}} = 150$ km/s, $N_{\text{HI}} = 4 \times 10^{19}$ cm $^{-2}$, $\tau_a = 3$, $b = 40$ km/s, $W(\text{Ly}\alpha)_0 = 50$ Å, $FWHM(\text{Ly}\alpha)_0 = 150$ km/s. We now compare these numbers to what other constraints are available.

The inferred expansion speed is close to the mean velocity derived from the LIS UV absorption lines $v_{\text{LIS}} = -100$ km/s (Rivera-Thorsen et al. 2014 in prep). Therefore, even though the LIS lines show a broad profile, extending over > 300 km/s, the idealized single shell model with the expansion speed equal to the mean v_{LIS} appears to be a reasonable approximation. The H α FWHM from SDSS (corrected for instrumental dispersion) is ~ 170 km/s, and $FWHM(\text{Ly}\alpha)_0$ is expected to be identical. The dust reddening inferred from the SDSS spectroscopy is $E_{B-V} = 0.09$ (Table 3) while the imaging

analysis suggests a nebular reddening of $E_{B-V} = 0.14$. In general spectroscopic measurements should be more accurate, but this has not been corrected for underlying Balmer absorption (which the imaging data has within LaXs). Converted to the optical depth in the vicinity of Ly α , the SDSS value represents $0.5 < \tau_a < 2$, depending on the extinction law applied (Calzetti et al. 1994; Cardelli et al. 1989; Prevot et al. 1984), while the imaging data suggest $0.8 < \tau_a < 2.8$. Our automated fit of the Ly α profile provided $\tau_a = 3$, which suggests that the dust composition of LARS#1 is more akin to the SMC bar (Prevot et al. 1984), and in particular has significantly more UV extinction than predicted by the Calzetti et al. (1994) attenuation law. The excess of UV extinction may also be an indication that the amounts of dust in HII and HI regions, inferred from the Balmer emission decrement and the Ly α line profile, respectively, are not identical.

No constraints are available for the Doppler parameter b or the HI column density N_{HI} . The gas-to-dust ratio derived from the N_{HI} obtained by the Ly α fitting is lower than the Galactic value $N_{\text{HI}}/E_{B-V} = 5.8 \times 10^{21} \text{ cm}^{-2}$ (Bohlin et al. 1978). However, as discussed earlier (Schaerer & Verhamme 2008; Verhamme et al. 2008b), the Ly α profile, sensitive to the HI outflow, may trace only a fraction of the total neutral hydrogen content, and thus N_{HI} derived from the Ly α emission line profile may not be representative of the entire HI content.

To estimate $W(\text{Ly}\alpha)_0$ we used the SDSS H α flux (Tab. 3) and the UV continuum flux in the vicinity of Ly α , measured from the COS data (corrected for the size difference of the apertures). We corrected the H α flux for reddening using the SDSS value, and the UV flux with τ_a derived from the optical SDSS value converted to UV by the extinction law. Scaling the extinction corrected H α flux with 8.7 we arrive at the predicted Ly α flux within the aperture, which divided by the corrected UV flux gives $W(\text{Ly}\alpha)_0 = 30 - 100 \text{ \AA}$ depending on the extinction law applied.

We conclude that the expanding homogeneous shell models capture the essential features of the Mrk 259 Ly α line profile, with no a-priori constraints applied. In addition, the ISM parameters characterising the best-fitting model are mostly consistent with those derived from independent data. Further detailed modelling exploring other possible solutions and their degeneracies will be presented in Orlitová et al. (2014, in preparation) for the entire LARS sample.

7. CONCLUSIONS AND SUMMARY

In this paper we have presented the Lyman Alpha Reference Sample (LARS), its survey outline and the powerful source of information that the combination of multiwavelength imaging and spectroscopy produce for understanding the Ly α production in the test-bench galaxy Mrk259. LARS comprises 14 galaxies and is the first comprehensive Ly α imaging study performed at low redshifts with a well defined selection function.

The study has been performed with the Hubble Space Telescope and with the Solar Blind Channel (SBC) of the Advanced Camera for Surveys (ACS), which is capable of imaging at the rest wavelength of Ly α . With ancillary imaging we also collected u, b, i , H α and H β with the UVIS channel of the Wide Field Camera 3 (WFC3) and

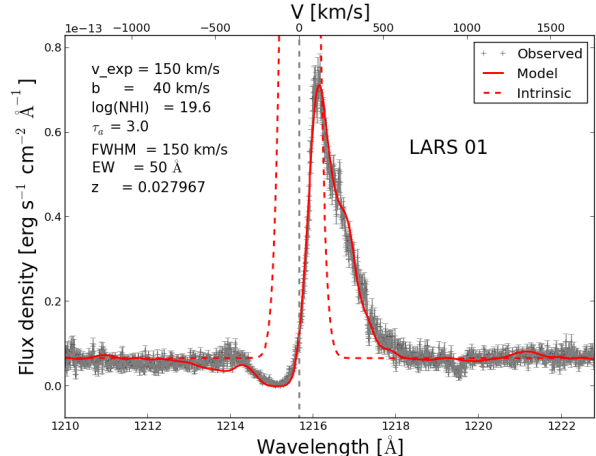


Figure 14. Best-fitting model of the Ly α emission-line profile, using the radiative transfer code. The observational data are plotted in black, the final model in solid red, and the intrinsic Gaussian Ly α profile (i.e., input in the radiative transfer code) in dashed red. The intrinsic profile has been artificially shifted down, to appear in the plotted scale. Therefore, the difference in the levels of the intrinsic and observed continuum does not correspond to the dust attenuation derived. A Milky-Way absorption line is visible in the red wing, masked for the Ly α profile fitting.

the Wide Field Camera (WFC) of ACS.

The targets were selected from the combined SDSS DR6 + GALEX DR3 catalogue. In order to study systems with significant production of Ly α photons, whether or not these escape, we applied a cut in the H α emission equivalent width of $W(\text{H}\alpha) \geq 100 \text{ \AA}$. Potential targets classified as AGN based on the width and ratios of emission lines were removed in order to focus on systems dominated by star formation. Objects with high foreground extinction were discarded.

Ly α imaging necessitates continuum subtraction which is non-trivial due to the strong evolution of the continuum near Ly α as a function of dust absorption and stellar population age. For low redshifts there is an additional complication in that the available continuum filters of HST are broad in comparison to the typical Ly α emission line equivalent width, and moreover sample continuum at significantly longer wavelengths than Ly α . Therefore we have developed the LARS eXtraction software (LaXs) that utilises UV and optical continuum filters and H α and H β images to perform a pixel-based SED fit in order to estimate the continuum at Ly α .

Targets were selected in two redshift windows ($z = 0.028 - 0.109$ and $0.134 - 0.190$) that allows Ly α to be captured with a combination of long pass filters in SBC that don't transmit the geocoronal Ly α line, offering a significantly improved sensitivity compared to the available $z \sim 0$ Ly α filter (F122M) in SBC.

In order to provide a useful comparison sample, we strived to cover a range of far UV (FUV) luminosities that is similar to the range observed for high ($z > 2$) redshift Ly α emitters and Lyman Break Galaxies. To provide maximum spatial resolution, preference was given to sources towards the lower end of the redshift range, but since luminous galaxies are intrinsically rarer, higher redshift sources were included in order to populate the high luminosity bins. When galaxies with available and relevant archival HST UV/visual imaging, or ex-

isting/planned COS spectroscopy, satisfied our selection criteria, these were give priority in order to lower the orbit request and increase the scientific value of the dataset. Twelve of the targets fall in the low- z window and two in the high- z one. Seven targets have archival COS spectroscopy, and the remainder were approved in Cycle 19 meaning that all LARS galaxies have both HST Ly α imaging and spectroscopy. In addition several projects to enhance the LARS dataset with other relevant data (optical IFU spectroscopy of the ionized gas kinematics, HI single dish and interferometric observations, far IR and CO observations, deep ground based optical and near IR imaging) are underway and will be the subject of future LARS papers.

In the current paper we also presented Ly α imaging and COS spectroscopy results for Mrk 259 (LARS #1), the first galaxy in the LARS sample. This galaxy is metal-poor and has a very extended asymmetric Ly α halo with strong emission in the north-eastern parts of the galaxy, and absorption in the south-western components. The remote emission regions have very high Ly α equivalent widths and Ly α /H α ratios suggesting that those Ly α photons have been resonantly scattered from the more centrally located star forming regions. The very highest UV surface brightness regions show Ly α in absorption. While the far UV continuum radial surface brightness profile is well fitted by a Sersic $n = 4$ profile the Ly α profile is purely exponential, and the Ly α escape fraction is seen to be monotonically increasing. The integrated Ly α luminosity is $\log(L_{Ly\alpha}) = 42.1$ erg/s/cm 2 and the equivalent width is 45 Å meaning that it would be detectable in high- z Ly α imaging surveys. The integrated Ly α escape fraction is 12%, an unusually high value for low redshift galaxies. The COS spectroscopy displays a Ly α emission line from the centre with a p-Cyg profile and blue shifted ISM absorption lines, indicating outflow of neutral gas. A radiative transfer model with a homogeneous expanding shell is able to reproduce the line profile with parameters that are in overall agreement with those that we derive from the Ly α imaging and SDSS spectroscopy.

As we have argued, a better physical understanding of what regulates the ability (or not) of a galaxy to emit the Ly α photons that are produced in its star-forming regions, is required in order to be able to reliably use Ly α as a probe of cosmology and the evolution of the galaxy population. The LARS project provides an important step along this line and is, as the name implies, intended to produce a local reference sample for aiding interpretation of high redshift Ly α studies where information is often scarcer. A number of papers have been/or are in

the process of being written: A letter (LARS paper 0) presented the ubiquitous extended Ly α haloes seen in the majority of the sample is already published (Hayes et al. 2013). Paper II (Hayes et al. 2014) presents further information on the large scale Ly α properties, paper III (Pardy et al. 2014, accepted) integrated HI masses, paper IV (Rivera-Thorsen et al. 2014 in prep) will focus on the ISM kinematics as inferred from COS spectroscopy, paper V (Duval et al 2014b, in prep) a detailed study of LARS#5, paper VI (Orlitova et al. 2014, in prep) radiative transfer modelling, paper VII (Guaita et al. 2014, in prep) a morphological analysis including the predicted appearance of LARS galaxies at high redshift. Subsequent papers will address IFU data from the Potsdam Multi Aperture Spectrometer (PMAS, Roth et al. 2005), HI interferometry from JVLA and GMRT, CO observations, optical/IR imaging, integrated SED fits, clumpy ISM RT models, etc, and a community data release.

In HST cycle 21 an extension of LARS, eLARS, was approved. Compared to LARS it is twice as big, comprising 28 targets, and with the $W(H\alpha)$ cut reduced to 40Å in order to provide more galaxies that fall along the star formation main sequence at low and high- z . COS spectroscopy for the full sample was furthermore approved in cycle 22.

This research has made use of the NASA/IPAC Extragalactic Database (NED) which is operated by the Jet Propulsion Laboratory, California Institute of Technology, under contract with the National Aeronautics and Space Administration. This work was supported by the Swedish Research Council (VR) and the Swedish National Space Board (SNSB). GÖ is a Royal Swedish Academy of Science research fellow (supported by a grant from the Knut & Alice Wallenbergs foundation). HA and DK acknowledge support from the Centre National d'Etudes Spatiales (CNES). HA is supported by the European Research Council (ERC) advanced grant Light on the Dark (LIDA). PL acknowledges support from the ERC-StG grant EGGS-278202. IO acknowledges the Sciex fellowship of Rectors Conference of Swiss Universities, grant 14-20666P of Czech Science Foundation, and the long-term institutional development grant RVO:67985815. MMR acknowledges support from BMBF under grant no. 03Z2AN11. HOF is funded by a postdoctoral UNAM grant. PL acknowledges support from the ERC-StG grant EGGS-278202. DK has been financially supported by the CNES.

Facilities: HST (ACS,WFC3,COS), SDSS.

APPENDIX

A 1. NGC 6090 – PROOF OF CONCEPT

For the starburst galaxy NGC 6090, at $z = 0.029$, there are HST images taken both with F122M (from GO program 9470, PI Kunth), and F125LP (program 11110 by PI McCandliss) as well as F140LP (both programs). In addition there are near UV and optical broadband and H α images from program 10575 (PI Östlin) and the results from programs 9470+10575 are presented in Östlin et al. (2009). This galaxy hence offers the opportunity to verify the new method using the long-pass filter combination, and compare it to our previous approach using F122M. In Fig. 15 we perform this comparison. The left panel shows the resulting Ly α image when F122M is used to capture the line, and the second panel from the left shows result when the F125LP–F140LP combination is used. The following panels show the H α image and the F140LP continuum images. A comparison of the results show that the use of F125LP increases the S/N with a factor of ~ 7 despite the exposure time being three times smaller, which can be attributed to the factor 5

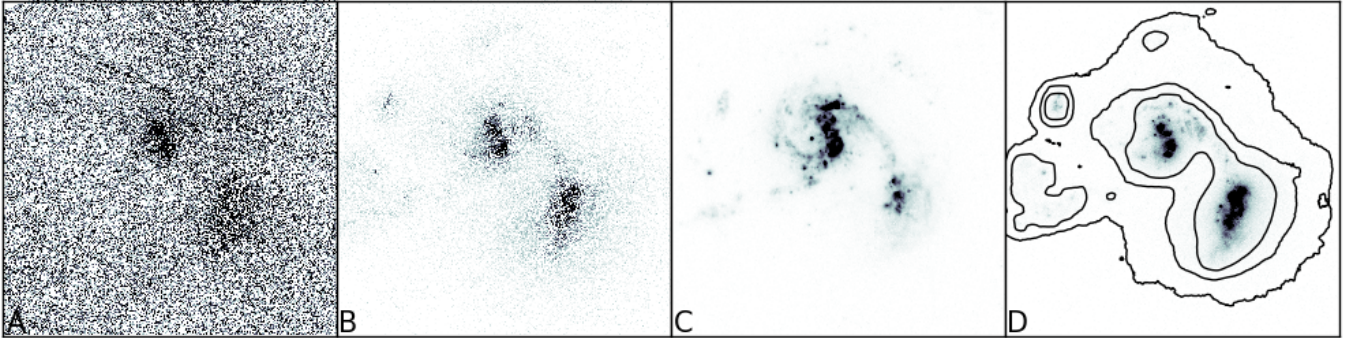


Figure 15. NGC6090: Comparison of results obtained for NGC6090 ($z = 0.029$) with F122M vs F125LP–F140LP. From left to right: **A** Ly α image produced from F122M observations (Östlin et. al. 2009); **B** Ly α image produced by using archival F125LP and F140LP data (PI McCandliss, program 11110) and the method described in Hayes et. al. 2009; **C** H α image; and finally **D** F140LP image with F140LP contours overlaid (image in C and D are from Östlin et al 2009). While the integrated photometry of the two Ly α images are fully consistent, the improvement in image quality is striking, amounting to an increase in the S/N of a factor of 7. Also for this galaxy is Ly α much more diffuse than H α or the UV continuum.

improvement in throughput combined with the background being a factor of 20 lower during the part of the orbit in which HST is in earth's shadow.

A 2. RE-CALIBRATING THE BANDPASSES OF THE SOLAR BLIND CHANNEL

We compared the fluxes measured by synthetic photometry in the COS/G130M and SDSS spectra, to those measured by standard aperture photometry in matched apertures of the HST images, using PySynphot. In doing so we found remarkable agreement between HST/WFC3 optical photometry and spectral photometry from the SDSS – discrepancies no larger than a few per cent were discovered, even in the narrowband filters. However when comparing the ACS/SBC aperture-matched flux densities with those obtained by spectral photometry in the COS/G130M spectrum, substantial differences were noticed. Specifically, the fluxes measured in the SBC imaging were systematically brighter, which persisted after accounting for vignetting in the Primary Science aperture of COS. Furthermore, a noticeable wavelength dependency was noticed in the discrepancy, which increases towards the blue, and its magnitude amounts to 11% in F150LP, 13% in F140LP, and 22% in F125LP. According to the instrument handbooks for COS and SBC, we can expect absolute accuracies to be better than 10% (COS) and 3% (SBC); our discrepancy at F125LP is double this combined difference, and while formally consistent in F140LP and F150LP, the offset is suspicious and a cause for concern.

Note that the vignetting correction depends upon the distribution of light within the PSA, and the correction for the continuum may be different from Ly α , which can be more extended. Ly α is transmitted only by F125LP, where the discrepancy is seen to be largest, so we also computed a vignetting correction for a flat surface that fills the aperture and applied it to the Ly α region of the COS spectrum. However the F125LP bandpass is so broad that this correction can account for no more than 1% absolute, or 4% of the relative offset seen in F125LP. I.e. COS vignetting is only a minor contributor to the photometric discrepancy.

Assuming that the cause of the discrepancy lies with one instrument alone, it can be explained if either COS (or SBC) becomes systematically less (more) sensitive than expected with decreasing wavelength. Specifically with respect to SBC, this could be attributed to either the response of the MAMA detector or the throughput of the filters. Unfortunately even with the extensive sets of calibration data that have been obtained, not one single object from the COS calibration data-sets has been observed with SBC imaging in the same filters that we have used. However, a rather complete SBC calibration campaign has been carried out, targeting the globular cluster NGC 6681 in all filters, and also with both PR110L and PR130L low resolution siltless prism spectroscopy. Thus for a substantial number of stars, the possibility exists to test the response of SBC against itself in imaging and spectroscopic modes.

The philosophy behind this experiment is as follows. The SBC LP bandpasses are defined on the red side by the sensitivity of the MAMA detector, which decreases with increasing wavelength. On the blue side they are described by a sharp cut on; thus all filters in principle share identical red-wings, which, modulo the prism response function, applies also in the two spectroscopic modes. The SBC has a well-known red leak, but the same principle applies here: each mode should be subject to the same leak, and its contribution to the integrated countrate should be the same in every case. Were the photometric discrepancy that we notice attributable to the red leak, it would not become more pronounced for the bluer filters.

We obtained the SBC data for NGC 6681 from the archive, opting to use 2009 calibration epoch; we obtained images in F125LP (data-sets ja8v02c7q and ja8v02e8q), F140LP (ja8v03imq and ja8v03inq), and F150LP (ja8v02c5q and ja8v02c6q), and prism spectral images in PR110L (ja8v02c3q and ja8v02c4q) which extends all the way across the F125LP bandpass. Using aXe V2.3 software (Kümmel et al. 2006) and SExtractor (Bertin & Arnouts 1996), we performed a spectral extraction of 80 objects. We first identified and extracted the sources in each individual direct image. The object positions are then used for the trace calculation and the wavelength calibration of the corresponding prism image. We used the prism reference files from cycle 13 and adopted a constant extraction direction, local background subtraction, and aperture size of 13 pixels. We then re-gridded and combine the two spectra extracted for

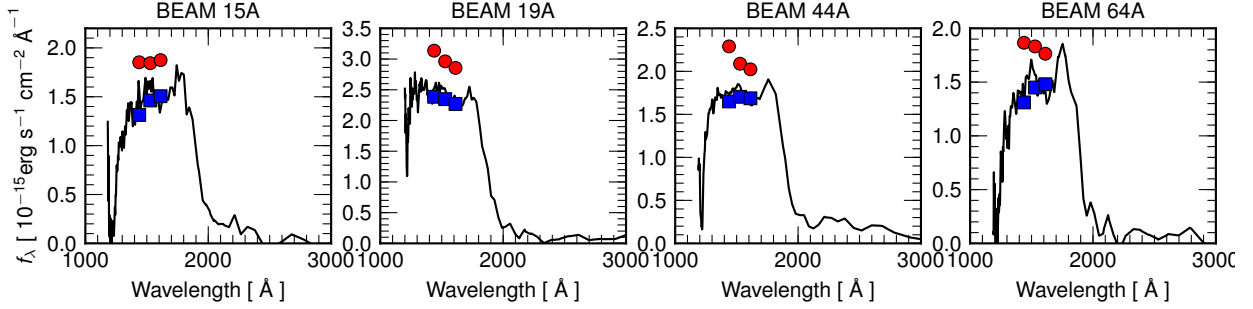


Figure 16. SBC/PR110L spectra for four representative stars in NGC 6681. Black lines show the spectra, while synthetic photometry performed on these spectra are shown by blue squares. Direct aperture photometry on the images is shown by red circles. Filters from short to long wavelength are F125LP, F140LP, and F150LP. There is an undoubtable systematic trend for fluxes measured in the images to exceed those measured in the spectra, and furthermore, the magnitude of this effect appears stronger in the bluer filters.

each star. We examined the stamps of the spectral extractions and remove any spectra that are not well-centered in the aperture, and any objects for which the projection of a nearby star falls near enough to contaminate the main spectrum. We further restrict our analysis only to objects that appear relatively blue in the calibrated low resolution spectrum (approximately $\beta < 1$); this is to insure that the majority of the counts in the images comes from the spectral region covered by the bandpass and not the red leak. We are then left with 20 stars. Using PySynphot we convolve these spectra with the F125LP, F140LP, and F150LP bandpasses, and measure the total flux that would hypothetically be seen in imaging mode.

We then perform aperture photometry of the same stars, using custom scripts. The spectral extractions described above use 13 pixel apertures on the cross-dispersion direction, but are essentially infinite in the dispersion direction, at least for photometric purposes. We therefore do our photometry in non-standard rectangular slit-like apertures, 13 native pixels high, and 1 arcsec (33 pixels) in length. This is to get a reasonable picture of total flux that will be throughput in spectroscopic mode. Figure 16 shows the fluxes obtained through spectroscopic and photometric measurements of a few representative stars from the sample.

Figure 16 shows a clear systematic: fluxes measured directly by aperture photometry in the images exceed those measured by synthetic spectrophotometry in the same filters. The effect appears more pronounced in the bluer filters, and decreases towards the red. For whatever reason, this is exactly the same phenomenon that we saw when comparing the SBC photometry to that of COS. The offsets for each filter are shown in Figure 17. Without applying any outlier rejection, we compute the luminosity-weighted average ratio to be for each of the three filters: F125LP: 1.193 ± 0.053 , F140LP: 1.113 ± 0.047 , F150LP: 1.126 ± 0.074 . When calibrating our science data we rescale the fluxes measured in the images down by these factors.

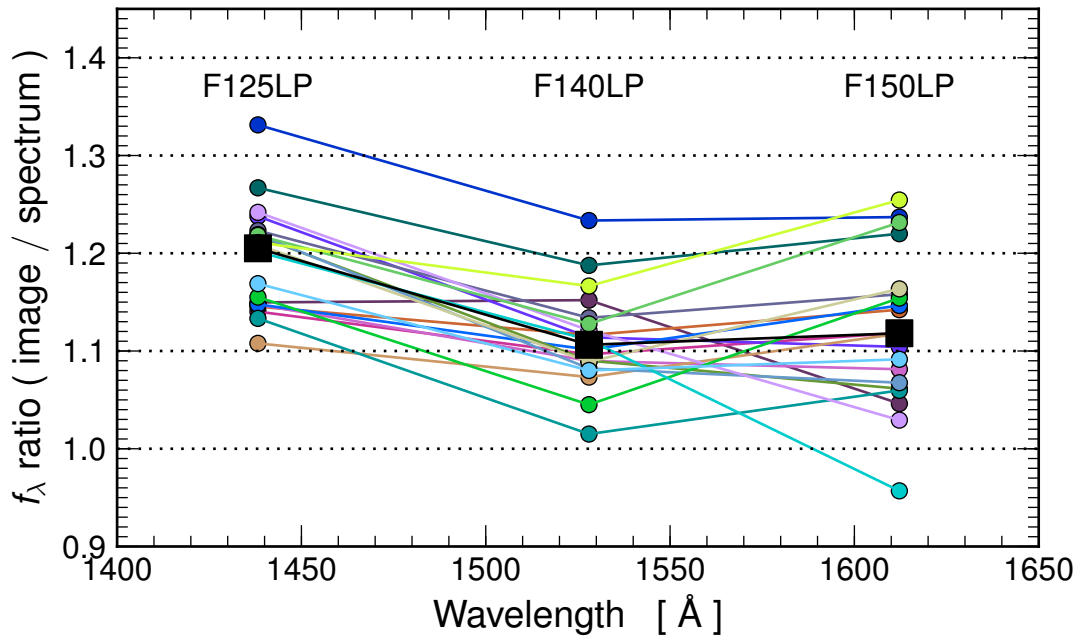


Figure 17. The relative corrections factors, defined as $\text{flux}(\text{image})/\text{flux}(\text{spectrum})$ for the 20 stars in NGC 6681 (coloured circles). The large black squares show the luminosity-weighted average ratio.

We note finally that our approach does not completely debug the photometric issue, but does reconcile SBC and COS

spectrophotometry to within the relative calibration levels of the COS. More dedicated work on the cross-calibration of these two instruments would be needed to fully resolve it.

REFERENCES

- Adams, J. J., Blanc, G. A., Hill, G. J., et al. 2011, ApJS, 192, 5
 Aller, L. H., ed. 1984, Astrophysics and Space Science Library, Vol. 112, Physics of thermal gaseous nebulae
 Anders, P. & Fritze-v. Alvensleben, U. 2003, A&A, 401, 1063
 Atek, H., Kunth, D., Hayes, M., Östlin, G., & Mas-Hesse, J. M. 2008, A&A, 488, 491
 Atek, H., Kunth, D., Schaerer, D., et al. 2009, A&A, 506, L1
 Atek, H., Kunth, D., Schaerer, D., et al. 2014, A&A, 561, A89
 Baldwin, J. A., Phillips, M. M., & Terlevich, R. 1981, PASP, 93, 5
 Bergvall, N. & Östlin, G. 2002, A&A, 390, 891
 Bertin, E. & Arnouts, S. 1996, A&AS, 117, 393
 Bigiel, F. & Blitz, L. 2012, ApJ, 756, 183
 Bohlin, R. C., Savage, B. D., & Drake, J. F. 1978, ApJ, 224, 132
 Bouwens, R. J., Illingworth, G. D., Oesch, P. A., et al. 2014, ArXiv e-prints
 Brinchmann, J., Charlot, S., White, S. D. M., et al. 2004, MNRAS, 351, 1151
 Calzetti, D., Kinney, A. L., & Storchi-Bergmann, T. 1994, ApJ, 429, 582
 Cantalupo, S. & Porciani, C. 2011, MNRAS, 411, 1678
 Cappellari, M. & Copin, Y. 2003, MNRAS, 342, 345
 Cardelli, J. A., Clayton, G. C., & Mathis, J. S. 1989, ApJ, 345, 245
 Chapman, S. C., Blain, A. W., Smail, I., & Ivison, R. J. 2005, ApJ, 622, 772
 Charlot, S. & Fall, S. M. 1993, ApJ, 415, 580
 Cowie, L. L., Barger, A. J., & Hu, E. M. 2010, ApJ, 711, 928
 Cowie, L. L. & Hu, E. M. 1998, AJ, 115, 1319
 Curtis-Lake, E., McLure, R. J., Pearce, H. J., et al. 2012, MNRAS, 422, 1425
 Deharveng, J.-M., Small, T., Barlow, T. A., et al. 2008, ApJ, 680, 1072
 Dessauges-Zavadsky, M., D'Odorico, S., Schaerer, D., et al. 2010, A&A, 510, A26
 Diehl, S. & Statler, T. S. 2006, MNRAS, 368, 497
 Dijkstra, M., Haiman, Z., & Spaans, M. 2006, ApJ, 649, 14
 Dijkstra, M. & Wyithe, J. S. B. 2010, MNRAS, 408, 352
 Duval, F., Schaerer, D., Östlin, G., & Laursen, P. 2014, A&A, 562, A52
 Elbaz, D., Dickinson, M., Hwang, H. S., et al. 2011, A&A, 533, A119
 Fan, X., Carilli, C. L., & Keating, B. 2006, ARA&A, 44, 415
 Gawiser, E., van Dokkum, P. G., Gronwall, C., et al. 2006, ApJ, 642, L13
 Giavalisco, M., Koratkar, A., & Calzetti, D. 1996, ApJ, 466, 831
 Gronwall, C., Ciardullo, R., Hickey, T., et al. 2007, ApJ, 667, 79
 Haiman, Z. 2002, ApJ, 576, L1
 Hansen, M. & Oh, S. P. 2006, MNRAS, 367, 979
 Hashimoto, T., Ouchi, M., Shimasaku, K., et al. 2013, ApJ, 765, 70
 Hayes, M., Östlin, G., Atek, H., et al. 2007, MNRAS, 382, 1465
 Hayes, M., Östlin, G., Duval, F., et al. 2014, ApJ, 782, 6 (paper II)
 Hayes, M., Östlin, G., Mas-Hesse, J. M., & Kunth, D. 2009, AJ, 138, 911
 Hayes, M., Östlin, G., Mas-Hesse, J. M., et al. 2005, A&A, 438, 71
 Hayes, M., Östlin, G., Schaerer, D., et al. 2010, Nature, 464, 562
 Hayes, M., Östlin, G., Schaerer, D., et al. 2013, ApJ, 765, L27
 Hayes, M., Schaerer, D., Östlin, G., et al. 2011, ApJ, 730, 8
 Heckman, T. M., Hoopes, C. G., Seibert, M., et al. 2005, ApJ, 619, L35
 Hoopes, C. G., Heckman, T. M., Salim, S., et al. 2007, ApJS, 173, 441
 Hu, E. M. & McMahon, R. G. 1996, Nature, 382, 231
 Hummer, D. G. & Storey, P. J. 1987, MNRAS, 224, 801
 Kauffmann, G., Heckman, T. M., White, S. D. M., et al. 2003, MNRAS, 341, 33
 Kennicutt, Jr., R. C. 1998, ARA&A, 36, 189
 Kümmel, M., Larsen, S. S., & Walsh, J. R. 2006, in The 2005 HST Calibration Workshop: Hubble After the Transition to Two-Gyro Mode, ed. A. M. Koekemoer, P. Goudfrooij, & L. L. Dressel, 85
 Kunth, D., Leitherer, C., Mas-Hesse, J. M., Östlin, G., & Petrosian, A. 2003, ApJ, 597, 263
 Kunth, D., Lequeux, J., Sargent, W. L. W., & Viallefond, F. 1994, A&A, 282, 709
 Kunth, D., Mas-Hesse, J. M., Terlevich, E., et al. 1998, A&A, 334, 11
 Laursen, P., Duval, F., & Östlin, G. 2013, ApJ, 766, 124
 Laursen, P., Sommer-Larsen, J., & Andersen, A. C. 2009, ApJ, 704, 1640
 Lehnert, M. D., Nesvadba, N. P. H., Cuby, J.-G., et al. 2010, Nature, 467, 940
 Leitherer, C., Chandar, R., Tremonti, C. A., Wofford, A., & Schaerer, D. 2013, ApJ, 772, 120
 Leitherer, C., Schaerer, D., Goldader, J. D., et al. 1999, ApJS, 123, 3
 Lequeux, J., Kunth, D., Mas-Hesse, J. M., & Sargent, W. L. W. 1995, A&A, 301, 18
 Lidman, C., Hayes, M., Jones, D. H., et al. 2012, MNRAS, 420, 1946
 Malhotra, S. & Rhoads, J. E. 2002, ApJ, 565, L71
 Malhotra, S. & Rhoads, J. E. 2004, ApJ, 617, L5
 Mallory, R. P., Mobasher, B., Capak, P., et al. 2012, ApJ, 760, 128
 Martins, F., Schaerer, D., & Hillier, D. J. 2005, A&A, 436, 1049
 Mas-Hesse, J. M. & Kunth, D. 1999, A&A, 349, 765
 Mas-Hesse, J. M., Kunth, D., Tenorio-Tagle, G., et al. 2003, ApJ, 598, 858
 Meurer, G. R., Heckman, T. M., & Calzetti, D. 1999, ApJ, 521, 64
 Neufeld, D. A. 1991, ApJ, 370, L85

- Nilsson, K. K., Møller, P., Möller, O., et al. 2007, A&A, 471, 71
 Nilsson, K. K., Tapken, C., Møller, P., et al. 2009, A&A, 498, 13
 Östlin, G., Hayes, M., Kunth, D., et al. 2009, AJ, 138, 923
 Ouchi, M., Shimasaku, K., Akiyama, M., et al. 2008, ApJS, 176, 301
 Overzier, R. A., Heckman, T. M., Kauffmann, G., et al. 2008, ApJ, 677, 37
 Prevot, M. L., Lequeux, J., Prevot, L., Maurice, E., & Rocca-Volmerange, B. 1984, A&A, 132, 389
 Reddy, N. A., Steidel, C. C., Pettini, M., et al. 2008, ApJS, 175, 48
 Roth, M. M., Kelz, A., Fechner, T., et al. 2005, PASP, 117, 620
 Salim, S., Rich, R. M., Charlot, S., et al. 2007, ApJS, 173, 267
 Salzer, J. J., Gronwall, C., Lipovetsky, V. A., et al. 2001, AJ, 121, 66
 Santos, M. R. 2004, MNRAS, 349, 1137
 Scarlata, C., Colbert, J., Teplitz, H. I., et al. 2009, ApJ, 704, L98
 Schaerer, D. & de Barros, S. 2009, A&A, 502, 423
 Schaerer, D. & de Barros, S. 2010, A&A, 515, A73+
 Schaerer, D., Hayes, M., Verhamme, A., & Teyssier, R. 2011, A&A, 531, A12
 Schaerer, D. & Verhamme, A. 2008, A&A, 480, 369
 Shapley, A. E., Steidel, C. C., Pettini, M., & Adelberger, K. L. 2003a, ApJ, 588, 65
 Shapley, A. E., Steidel, C. C., Pettini, M., & Adelberger, K. L. 2003b, ApJ, 588, 65
 Shimasaku, K., Kashikawa, N., Doi, M., et al. 2006, PASJ, 58, 313
 Stark, D. P., Ellis, R. S., Chiu, K., Ouchi, M., & Bunker, A. 2010, MNRAS, 408, 1628
 Steidel, C. C., Giavalisco, M., Dickinson, M., & Adelberger, K. L. 1996, AJ, 112, 352
 Tapken, C., Appenzeller, I., Noll, S., et al. 2007, A&A, 467, 63
 Tasitsiomi, A. 2006, ApJ, 645, 792
 Tenorio-Tagle, G., Silich, S. A., Kunth, D., Terlevich, E., & Terlevich, R. 1999, MNRAS, 309, 332
 van Breukelen, C., Jarvis, M. J., & Venemans, B. P. 2005, MNRAS, 359, 895
 Vanzella, E., Giavalisco, M., Dickinson, M., et al. 2009, ApJ, 695, 1163
 Vanzella, E., Grazian, A., Hayes, M., et al. 2010, A&A, 513, A20
 Vázquez, G. A. & Leitherer, C. 2005, ApJ, 621, 695
 Verhamme, A., Dubois, Y., Blaizot, J., et al. 2012, A&A, 546, A111
 Verhamme, A., Schaerer, D., Atek, H., & Tapken, C. 2008a, A&A, 491, 89
 Verhamme, A., Schaerer, D., Atek, H., & Tapken, C. 2008b, A&A, 491, 89
 Verhamme, A., Schaerer, D., & Maselli, A. 2006, A&A, 460, 397
 Wofford, A., Leitherer, C., & Salzer, J. 2013, ApJ, 765, 118
 Yajima, H., Li, Y., Zhu, Q., & Abel, T. 2012, MNRAS, 424, 884
 Yin, S. Y., Liang, Y. C., Hammer, F., et al. 2007, A&A, 462, 535